A Multi-line aperture synthesis study of Orion-KL

M.C.H. Wright, R.L. Plambeck and D.J. Wilner[1]
Radio Astronomy Laboratory, University of California, Berkeley, CA 97420

ABSTRACT

We have mapped the Orion-KL region in 28 transitions of 16 molecular species (H_2CO, DCN, HDO, CH_3CH_2CN, HC_3N, SO_2, OCS, ^{29}SiO, SiO, SO, $H^{13}CN$, HCN, HCO^+, CH_3CN, CH_3OH, CO) near 3 millimeters wavelength using the BIMA array. The maps have $1'' - 6''$ angular resolution and $0.3 - 4$ km s^{-1} velocity resolution.

The images show two principal molecular concentrations in a ridge of dense gas, one toward the Kleinmann Low Nebula (KL), the other approximately $25''$ to the northeast, toward dust continuum source CS1. The "hot core", "compact ridge", and "plateau" spectral features all are associated with KL. This region has broad linewidths, high excitation emission, and unusual chemical abundances; it is associated with luminous infrared sources, masers, and a powerful bipolar outflow from at least one embedded young stellar object. By contrast, CS1 has narrower linewidths, lower temperatures, and only weak indications of star formation.

The maps provide evidence that the outflow from KL impacts and heats the southern edge of CS1. CH_3OH and CH_3CN emission peaks and a cluster of H_2O masers are seen here. The outflow may also be responsible for the velocity divergence of the ridge gas seen toward KL.

At $1''$ angular resolution the hot core appears as a chain of dense clumps offset approximately $1''$ east of radio continuum source I (IRc2). The HC_3N vibrational excitation temperature in the hot core is inferred to be 335 K.

The high abundance of HDO, DCN, and other deuterated species in the hot core indicates evaporation of icy grain mantles. CH_3OH, prominent in the compact ridge, appears to be liberated from the grain mantles at a lower temperature than H_2O, perhaps indicating that it is selectively evaporated from mixed molecular ices at ~ 120 K.

The "plateau" spectral feature looks quite different in different molecular tracers. Bright SiO v=0 emission appears to define a 1000 AU diameter flared disk around radio source I; weaker, thermal SiO emission appears to fill the infrared cavity around source I. SO and SO_2 form a shell of expanding gas, probably where the outflow shocks dense clumps along the periphery of the cavity. High velocity HCN and HC_3N emission seems to trace material ablated from these clumps.

---

[1]present address: Harvard-Smithsonian Center for Astrophysics, 60 Garden Street, Cambridge, MA 02138

The high velocity outflow probably originates from source I. It does not appear to be well-collimated, but instead expands in a wide angle cone. The outflow appears to be partially blocked to the southeast by the hot core clumps.

In an appendix, we present a table of column densities for each observed molecular species at 9 positions across the source, for comparison with chemical models. All the maps discussed in this paper are available in FITS format from the NCSA digital image library.

Subject headings: interstellar: molecules — stars: formation — nebulae: Orion nebula

1. Introduction

At 500 pc distance, the Kleinmann–Low Nebula in Orion is the closest region of massive star formation and has received extraordinary observational attention (see Genzel & Stutzki 1989 for a review). This region may be the Rosetta Stone that will help us understand what triggers the process of massive star formation and how this process disrupts the surrounding molecular cloud. Orion-KL has been the target of numerous millimeter wavelength molecular line surveys (e.g. Johansson et al. 1984, Sutton et al. 1985, Blake et al. 1986; Sutton et al. 1995), and it is now clear that this is a region of great chemical complexity as well as dynamical activity. The presence of embedded sources has radically altered the chemical abundances in the surrounding molecular material.

Emission from most of the spectral lines in Orion-KL originates in a region only $20'' - 30''$ in diameter, smaller than or comparable to the beamwidths of most radio telescopes. Consequently, much of the knowledge of this source is based on deconvolution of the line profiles into spectral components, such as the "ridge," "hot core," and "plateau." While this technique has led to impressive progress in understanding the chemistry of the cloud core, the deconvolutions are not unique and miss important morphological differences that only high resolution imaging can reveal. For example, the maps presented in this paper show that emission from lines of SiO and SO_2, despite the similarity of their "plateau" profiles, originate from spatially distinct regions. Since maps of different lines in Orion-KL often bear little resemblance to one another, high resolution observations of many species and transitions also are needed to develop a reliable model of the source structure and kinematics, even if one is uninterested in interstellar chemistry.

Erickson et al. (1982) first showed that the high velocity line wings seen toward KL originate from a bipolar outflow. Wright et al. (1983) mapped the SiO line wings with $6''$ resolution, and showed that the outflow origin was close to infrared source IRc2. More recent observations indicate that the infrared position for IRc2 is offset by $0.8''$ from the position of radio continuum source "I" and its associated SiO maser (Gezari 1992; Dougados et al. 1993; Menten & Reid 1995). The asymmetry of the SiO maser emission strongly hints that source I drives the bipolar outflow (Wright & Plambeck 1983; Wright et al. 1995). Source I may have a mass as high as 25 $M_{\odot}$ if it is the source of most of the 10^5 $L_{\odot}$ luminosity of the KL Nebula. A much lower mass is inferred from the rotation velocity of the SiO maser disk around source I, however; the rotation velocity is 10 km s^{-1} 40 AU from the star (Plambeck, Wright, & Carlstrom 1990), which implies a central mass of about 5 $M_{\odot}$.

Blake et al. (1987) provide a framework for understanding the chemistry of Orion-KL in terms of an oxygen rich outflow from IRc2. The detection of deuterated species toward the hot core prompted consideraton of the role of grain chemistry. NH_3 (Walmsley et al. 1987) and HCN (Mangum et al. 1991) show a D/H enrichment of more than 100 in the hot core, and HDO shows a similarly enhanced abundance towards the hot core and compact ridge (Plambeck & Wright 1987). The high abundance of deuterated molecules can be understood as the result of the recent evaporation of grain mantles which formed in cold regions where fractionation increases the deuterium abundance. Charnley, Tielens & Millar (1992) were able to reproduce the observed abundances of many molecules in the hot core and compact ridge with a model in which the grain mantle ices provided the required precursors for ion-molecule and neutral chemistry, primarily through the injection of NH_3 in the hot core and of CH_3OH in the compact ridge. Chemical differences between the hot core and compact ridge may also reflect differences in the thermal histories of these two regions (Caselli, Hasegawa, & Herbst 1993).

Over the last decade, we have used the BIMA array[2] to make aperture synthesis maps of Orion-KL in a large number of molecular lines near 3 millimeters wavelength. The BIMA array is particularly well-suited for high resolution mapping of Orion-KL because the $\sim 2'$ primary beamwidth of the array antennas comfortably encompasses the Kleinmann-Low Nebula and the surrounding molecular core. Hence the aperture synthesis observations recover all the flux in all but a few of the most extended lines. In 1993, following the expansion of the array from three to six antennas, we reobserved the SiO v=0 J=2–1 and SO 2_2-1_1 lines, obtaining in a few nights maps with greatly improved sensitivity and dynamic range compared with those laboriously obtained over entire seasons with the two antenna interferometer (Wright et al. 1983, Plambeck et al. 1982). The new maps provide an opportunity to bring together into one paper a compendium of Orion-KL molecular line observations obtained thus far with the BIMA array.

The paper is organized as follows. In §2 we describe the observational procedures used for the survey. In §3 we present the spectral images, with detailed notes on data not previously published. In §4 we discuss the overall picture of the source structure and kinematics that has developed from the high resolution observations. In an appendix, we present a table of LTE column densities derived at 9 positions for comparison with chemical models.

[2]The BIMA array is operated by the Berkeley-Illinois-Maryland Association under funding from the National Science Foundation

2. Observations

The data presented here were obtained between 1982 and 1995 with the BIMA array at the Hat Creek Radio Observatory. Prior to 1985, the array consisted of a two antenna interferometer. Spectra were obtained with two filter bank spectrometers, one of fifty 1.2 MHz wide channels, a second of sixty-four 250 kHz channels; these could be independently centered within the 400 MHz IF passband (Welch et al. 1981). In 1985 a third antenna was added, and the filter banks were replaced with a 512 channel digital correlator (Urry, Thornton, & Hudson 1985). Also in 1985, the phase-switching scheme was redesigned so that signals appearing the the receivers' upper and lower sidebands were separated in the correlator; the sideband isolation is about 30 dB. In 1993 the array was expanded to six antennas and a new 15 baseline digital correlator providing up to 2048 channels per baseline was installed. The correlator can be configured to sample all or part of an 800 MHz wide IF passband, with adjustable frequency resolution. This flexibility allows one to map a number of molecular lines at the same time, each with high spectral resolution, a big advantage for a source with many bright lines like Orion-KL.

The antennas are 6.1 meters in diameter, and can be stationed at any of 32 positions on a T-shaped track to achieve projected spacings ranging from 6 meters to 300 meters east-west and 200 meters north-south. In addition to these stations, the first two of several outrigger stations to provide a factor of three higher spatial resolution were brought into operation in 1994 December (Welch et al., 1996).

The telescopes are outfitted with a mix of Schottky and SIS receivers; DSB receiver temperatures range from 50–140 K. The SIS receivers are cooled to 3.5 K with novel Gifford-McMahon refrigerators (Plambeck, Thatte & Sykes 1993). A single Gunn oscillator on each antenna, tunable from 70 to 115 GHz, serves as the local oscillator (Carlstrom, Plambeck & Thornton 1985). The receiver gains are calibrated with the chopper wheel method (Ulich & Haas 1976). Single sideband system temperatures, corrected for atmospheric extinction, were typically 300–500 K for the Orion observations.

The pointing center for most of the observations was $\alpha = 05^h32^m47^s\!.0, \delta = -05°24'21''$ (B1950), although in a few cases we used the SiO maser position, $\alpha = 5^h32^m47''\!.026, \delta = -05°24'23''\!.88$ (B1950) measured by Wright et al. (1990). The primary beamwidth ranges from $2'\!.7$ at 70 GHz to $1'\!.7$ at 115 GHz.

For most of the observations, the quasars 0420–014 and 0528+134 were observed at 30 to 40 minute intervals as phase calibrators. The 1982 observations of SO and HCO^+ (Plambeck et al. 1982), and the 1993–95 observations of SO, $H^{13}CN$ and SiO used the SiO v=1 maser at 86.243 GHz as a gain and phase reference. Quasars 0420–014 and 0528+134 also were used as secondary amplitude calibrators, to determine the conversion factor from antenna temperature to flux density. Periodically, with the interferometer at compact configurations, the quasar flux densities were measured relative to planets assuming the planetary brightness temperatures given by Ulich (1981). We expect that the uncertainty in the absolute amplitude scale is approximately

$\pm 20\%$.

Phase and gain variations across the I.F. passband were calibrated in two steps. First, one of the antenna I.F. signals was coupled into all of the correlator inputs, and the correlator was commanded to perform a cross-correlation measurement. This yields an extremely high signal to noise measurement of the passband of the correlator filters in just 2 secs. Residual phase slopes attributable to the receivers vary much more slowly with frequency and are found to be quite stable with time. These are calibrated by observing a strong quasar (generally 3c273), or a planet at compact antenna configurations. This scan also calibrates out any inequalities in the receiver response to the upper and lower sidebands of the first local oscillator.

Maps were initially made with the UC Berkeley RALINT program, and more recently with the MIRIAD software package (Wright & Sault 1991). In most cases, several sets of maps were generated; naturally weighted maps (with all visibility data given equal weight) were used to search for extended emission; uniformly weighted maps (weighting inversely proportional to density in the u, v plane) were used to obtain the cleanest beam with highest spatial resolution. Maps were CLEANed with a flux cutoff of 1–2 times the theoretical rms noise limit. In some cases maps were also made using the Maximum Entropy algorithm (e.g. HCO^+, Vogel et al. 1984).

3. Results

Table 1 lists the molecular lines which were mapped, along with the dates of observation, assumed rest frequencies, beam sizes (uniform weight), and references to previous publications of these data. The rms noise level is typically 0.5 Jy beam^{-1} for a 1 km s^{-1} velocity interval; for a $4'' \times 4''$ synthesized beam, this corresponds to an rms brightness temperature of ~ 5 K. It's not practical to publish individual channel maps for all the molecular lines observed; however, multichannel images of all lines listed in Table 1 may be obtained in FITS format from the NCSA digital image library, accessible via URL ⟨ http://imagelib/ncsa.uiuc.edu/imagelib ⟩.

In discussing the images, it is convenient to refer to the conventional spectral components – "ridge,", "hot core," and so on – used to deconvolve single dish line profiles. Table 2 gives working definitions of the components adopted for this purpose, together with brief physical descriptions.

Figures 1–3 present images of the molecular distributions corresponding to the ridge, hot core, and compact ridge spectral components. The plateau component consists of a mixture of outflow, shocks, and interactions with the ambient cloud and is discussed in §4.5. The λ 3 mm continuum map of Wright et al. (1992), which traces thermal emission from dust, is included in Figures 1 and 3 for comparison with the molecular distributions. Dust emission at 3 mm is optically thin, and is relatively free from the effects of chemistry and excitation that influence the molecular emission; thus it serves as the best tracer of the total molecular column density. Examination of the figures shows that in general, the extended ridge follows the dust distribution, the hot core appears as a compact clump centered about $2''$ southeast of IRc2, and the compact ridge extends $10''$–$15''$ to the south and east of the hot core.

In the following sections, we summarize previously unpublished results for the species SiO, OCS, $H^{13}CN$, $HC^{15}N$, NH_2D, CH_3CH_2CN, HC_3N, SO, and SO_2.

3.1. SiO and ^{29}SiO

The v=1 J=2–1 transition of SiO is a strong maser. It is observed to be time variable but is dominated by two bright features that peak at velocities near −5 and +16 km s^{-1}. Wright et al. (1990) measured the absolute position of the maser to an accuracy of 0.″15. This position, $\alpha = 5^h32^m47.''026, \delta = -05°24'23.''88$ (B1950), coincides within the errors with that of radio continuum source I (Menten & Reid 1995, Plambeck et al. 1995).

Plambeck, Wright & Carlstrom (1990) showed that the individual maser velocity features lie in an 0.″15 diameter ring with a surprisingly regular velocity pattern. A simple model of maser emission from an expanding, rotating disk, roughly 80 AU in diameter, was able to reproduce this velocity pattern. This distribution of maser spots has since been confirmed by measurements with the Nobeyama and IRAM arrays (Morita et al. 1992; Guilloteau et al. 1992). A similar distribution is also observed in the SiO v=1 J=1–0 line (Menten & Reid 1995).

The v=0 J=2–1 transition of SiO is strongly peaked near IRc2. Early BIMA maps showed that the blueshifted and redshifted SiO line wings were asymmetrically distributed around IRc2, which suggested that IRc2 was the driving source of the outflow (Wright et al. 1983). New observations with much higher resolution described by Wright et al. (1995) show that the bright SiO emission is centered within 0.″1 of the SiO maser position and radio source I . The peak brightness temperature of 3700 K suggests that the ground state line may also be showing maser action. Figure 4 shows that the extended envelope of SiO emission does not trace the ridge, hot core, or any of the other spectral components, but instead appears to fill the interior of the shell traced by SO emission.

The ^{29}SiO v=0 J=2–1 emission is unresolved and centered at $\alpha = 05^h32^m47.^s00 \pm 0.^s013, \delta = -05°24'23.''8 \pm 0.''4$ (B1950). This is coincident within the errors with the SiO v=1 J=2–1 maser position, and the line emission spans the same velocity range. The peak brightness temperature is 80 ± 6 K in a 2.″4×4.″4 beam. Time variability and changes in narrow spectral features have been reported as evidence for maser emission in this line (Oloffsson et al. 1981).

3.2. OCS

J=7–6 OCS emission peaks south of the hot core and western clump. The maximum integrated intensity lies approximately 3″ southwest of IRc2. The line profile in this direction peaks at 8 km s^{-1} with brightness temperature 40 K. It is a mixture of compact ridge and hot core components; in addition, there is a weak pedestal with FWZP = 40 km s^{-1}. There is no sign of the eastern streamer of compact ridge emission so prominent in the HDO or CH_3OH maps. No OCS emission is detected at the northern dust peak.

3.3. $H^{13}CN$, $HC^{15}N$ and NH_2D

The 1993-95 observations of the $H^{13}CN$ line provide images with higher spatial resolution, velocity resolution, and dynamic range than the early images of the HCN main isotope reported by Vogel et al. (1985). $H^{13}CN$ emission follows the dust emission closely; the ridge, hot core, and compact ridge components can all be identified in $H^{13}CN$ emission in Figures 1–3. Figures 4 and 10 show higher resolution $H^{13}CN$ images which include data with baselines from 6–846 meters. With a $1\overset{''}{.}7 \times 0\overset{''}{.}7$ beam, the hot core is resolved into a number of clumps $1''$–$2''$ in size. These clumps are similar to those seen in VLA NH_3 observations with comparable spatial resolution (Migenes et al. 1989), but there is not a one-to-one correspondence between the $H^{13}CN$ and NH_3 peaks. Transitions of $HC^{15}N$ and NH_2D not previously observed in our survey were serendipitously measured with 86 GHz continuum observations (Plambeck et al. 1995), though with a velocity resolution of only 10 km s^{-1}. Maps of these lines (Figure 9) include only baselines from 97–846 m, and hence are sensitive only to structures less than about $8''$ in diameter.

3.4. CH_3CH_2CN

Ethyl cyanide (CH_3CH_2CN) emission is confined to a $\sim 12'' \times 10''$ region centered about $2''$ southeast of IRc2, coincident with the hot core dust emission peak. The peak brightness is 14 K in a 1.2 km s^{-1} channel. The line profiles are well fit by Gaussians with center velocity 4.5 ± 0.3 km s^{-1} and FWHM 7.0 ± 0.6 km s^{-1}, typical of the hot core.

3.5. HC_3N

We were able to make simultaneous observations of the J=9–8 HC_3N emission from both the ground and the ν_7 vibrational states. Maps of the ground state emission are shown in Figures 1–3. This emission can be traced over the full length of the ridge, from the north dust peak to the compact ridge in the south. The HC_3N emission also has a prominent peak a few arcseconds to the northwest of the BN object (Figure 1 and Figure 6), which is part of a clumpy filament also seen in $H^{13}CN$, CH_3CN (Wilner, Wright & Plambeck 1994), 400 μm continuum (Wright et al. 1992), and NH_3 emission (Murata et al. 1992).

A map of the ν_7 emission is shown in Figure 2. The ν_7 lines are 320 K above the ground state and can be used to estimate an excitation temperature in the hot core region as described in section 4.3.1. Since the peak brightness of the ν_7 lines is only 10 mK (main beam antenna temperature), comparable with the continuum emission from the hot core dust peak, it is necessary to very carefully subtract the continuum in order to obtain an accurate estimate of line strength. We did this in three ways, all of which gave similar results. The simplest method was to subtract an image of the continuum estimated from the adjacent correlator window. Since the continuum window was only 200 MHz from the line emission, the sidelobe pattern, which scales with frequency, was also closely subtracted. The second method was to subtract a model of the dust emission from the u, v data, for which we used the 3 millimeter bandwidth synthesis continuum image of Wright et al. (1992) for the model. The third method estimated the continuum from a least squares fit to the real and imaginary parts of the u, v data for each integration using the technique described by Cornwell et al. (1992). Over a small frequency range, the continuum emission gives real and imaginary parts in the u, v data which are linear functions of frequency. By excluding the line channels from the fit, we can subtract both the continuum and any residual passband slopes in the data. The third method provided the result with the highest dynamic range. The ν_7 line emission is centered on the hot core dust peak, with extensions to the west and south. The brightness temperature in a 10 km s^{-1} interval centered at 5 km s^{-1} is 20 K in a $3''.2\times3''.0$ beam.

3.6. SO and SO_2

The SO 2_2–1_1 and SO_2 $8_{1,7}$–$8_{0,8}$ maps closely resemble each other. The SO 2_2–1_1 line was mapped with $6''$ angular resolution by Plambeck et al. (1982), who modelled the SO emission as arising from an expanding ring, or "doughnut," of gas centered on IRc2. The newer maps have higher signal-to-noise and better spatial and spectral resolution than the 1982 data, and show that there are several spectral features within the doughnut. The quiescent gas is most apparent in the velocity range 10–14 km s^{-1}, which avoids the outflow and much of the hot core emission, centered at 5 km s^{-1}, but still shows contamination from the compact ridge to the southeast at 6–10 km s^{-1}. The observations of the SO line with $1''.7\times0''.7$ resolution show a remarkable shell of emission (Figure 4). Both the SO and SO_2 lines show prominent hot core and compact ridge components. SO emission extends farther toward the north dust peak; SO_2 emission extends farther to the southeast into the compact ridge.

4. Discussion

Figures 1–3 show dramatic differences in the spatial distributions of many of the molecular lines mapped in the BIMA survey. A question of primary importance is to what extent these differences are attributable to variations in chemical abundances, rather than excitation effects. Detailed radiative transfer models for each species, incorporating infrared excitation, are required to separate the roles of chemistry and excitation. Such a treatment, including detailed assumptions about the source geometry, is beyond the scope of this paper. However, for optically thin transitions with similar excitation requirements, major morphological differences must be dominated by chemistry. These conditions likely hold for most of transitions observed (with some obvious exceptions, for example the high optical depth HCN, HCO^+, and CO lines).

If one assumes that the observed transitions are optically thin and that the rotational energy levels for each species are thermalized at a single excitation temperature, then it is straightforward to convert the line intensities measured from the maps into total column densities along each line of sight. Unfortunately, even with an angular resolution of 6″ we found that the line profiles toward many positions were a blend of several spectral components, indicating the presence of gas with different physical conditions along the line of sight. Thus, we used a Gaussian fitting procedure to separate these components and calculated the column densities independently for each. The details of the fitting procedure and a table of the results will be found in Appendix A.

The images reveal two principal concentrations of gas in the mapped region: one near the Kleinmann-Low Nebula, with LSR velocity 8 km s^{-1}, the other $\sim$ 25″ to the northeast, with velocity 10.5 km s^{-1}. These two concentrations correspond to high density clumps inferred from dust continuum maps. Comparison of these two regions provides an interesting picture of the effect of massive star formation on the molecular environment. The southern concentration, with a total luminosity of $\sim 10^5\ L_\odot$, contains many embedded infrared sources and at least one powerful outflow. The molecular linewidths are large, 5–10 km s^{-1}, and the inferred kinetic temperatures are $\gtrsim$ 250 K. Emission from high excitation lines, masers, and other shock tracers are seen. By contrast, the northern concentration shows no evidence of massive star formation. The molecular linewidths are narrow, $\sim$ 1.5 km s^{-1}, and the inferred kinetic temperatures are lower, $\sim$ 50 K.

In the following sections, we discuss in turn the conventional Orion spectral components – ridge, northern cloud, hot core, compact ridge, and plateau. We describe the physical conditions, source structure, kinematics, and chemistry of each of these regions, as revealed by the multi-line high resolution maps.

4.1. Ridge: Rotation or Two Clouds?

Single-dish observations of many molecular species have established that the Kleinmann-Low nebula is embedded within a flattened molecular cloud which is extended along a northeast-southwest direction (e.g. H_2CO, Bastien et al. 1985; $C^{18}O$, Wilson et al. 1986). This molecular ridge is evident in the HCN, $H^{13}CN$, HC_3N, CH_3CN, and CH_3OH maps in Figure 1. Mundy et al. (1986) mapped the 95 GHz continuum and the CS J=2–1 line emission from a $2' \times 3'$ region along this ridge by overlapping observations of ten pointings of the OVRO millimeter array. They identified four major condensations within the ridge. Two of these, CS1 and CS2 ("continuum source" 1 and 2), lie within the BIMA field of view and are readily apparent in dust continuum emission (see Wright et al. 1992 and Figure 1). CS1 is associated with the northern cloud; CS2 with the Kleinmann-Low Nebula.

The LSR velocity of the molecular ridge gas shifts abruptly from 10.5 km s^{-1} northeast of KL to 8 km s^{-1} southwest of KL. It has long been controversial whether this velocity shift is caused by the presence of two (perhaps colliding) clouds along the line of sight (Ho & Barrett 1978; Bastien et al. 1985; Wang, Wouterloot, & Wilson 1993; Womack, Ziurys & Sage 1993) or differential rotation around KL (Hasegawa et al. 1984; Vogel et al. 1984; Murata et al. 1992).

The initial evidence for two separate clouds along the line of sight was based on observations with low angular resolution– 1.′3 for the NH_3 data of Ho and Barrett (1978) and 1′ for the H_2CO data of Bastien et al. (1985). More recent observations of CH_3CCH by Wang, Wouterloot & Wilson (1993) and N_2H^+ by Womack, Ziurys & Sage (1994) have higher resolution (29″ and 26″ respectively) but both of these species appear to be underabundant in the dense, warm gas near KL. It may be argued that this underabundance represents an advantage in tracing the ridge gas, because these lines are not contaminated by the broad velocity emission from the KL outflow. On the other hand, it means that these molecules are poor probes of the velocity field in the critical region within 10″–20″ of IRc2. At higher angular resolution, one finds that there is a *divergence* in the velocity of the ridge gas near KL: approaching from the south, the velocity decreases from 8 to about 6 km s^{-1}; approaching from the north, the velocity increases from 10 to about 11 km s^{-1}. This divergence was first seen in 6″ resolution BIMA maps of HCN (Vogel et al. 1984). It also is apparent in the 21″ resolution maps of the $C^{18}O$ J=1–0 line obtained with the IRAM 30 meter telescope (Wilson et al. 1986) and in 6″ resolution maps of CS J=1–0 emission from the Nobeyama Millimeter Array (Murata et al. 1992).

In Figure 5 we show position velocity cuts along position angle 23 degrees derived from the $H^{13}CN$, HC_3N, SO, and CH_3CN images. As with the HCN and CS emission, the velocity field within a 10″ region surrounding IRc2 is dominated by the high velocity outflow. The velocity divergence in the ridge gas is most evident 10″–20″ from IRc2. The rotation velocities fit by Vogel et al. (1984) to HCN are overlaid on Figure 5 for comparison; these are in reasonable agreement with the current data.

Vogel et al. (1984) and Murata et al. (1992) interpreted the velocity divergence as evidence for differential rotation around IRc2. The velocity field is consistent with rotation around a central mass of about 25 $M_\odot$ and a more extended mass distribution with $M(r) \propto r$. The total mass enclosed within a radius of 45″ is estimated to be 120 $M_\odot$ from dust continuum emission (Keene, Hildebrand & Whitcomb 1982). However, Wilson et al. (1986) suggested that the velocity divergence might be equally well explained by acceleration of the ambient ridge gas by the outflow from KL; this requires that the outflow is located between the 8 and 10 km s^{-1} clouds, with the 8 km s^{-1} cloud in the foreground.

Although our data do not distinguish conclusively between these possibilities, we believe that the outflow hypothesis of Wilson et al. (1986) is the more likely. In §4.2.3 below, we present evidence that the outflow from KL is plowing into the southern edge of the 10.5 km s^{-1} cloud.

The northern boundary of the interaction region is about 20″ northeast of IRc2, precisely where the velocity divergence becomes noticeable. Both continuum and spectral line emission is weak 10″ northeast of IRc2, consistent with the idea that the outflow has cleared away most of the ambient gas in this zone.

4.2. The Northern Cloud ("CS1")

The dust continuum peak labeled CS1 by Mundy et al. (1986) is within 2″ of the position determined by Wright et al. (1992), 25″ northeast of IRc2. Since this is well inside the half power point of the BIMA primary beam, no primary beam corrections have been made to the maps.

Figure 6 compares maps of the molecular line emission integrated over the narrow velocity range 9.5–11.5 km s^{-1} characteristic of the northern cloud. DCN, $H^{13}CN$, HC_3N, and CH_3CN are prominent in this direction, though the emission from these species peaks a few arcseconds to the south of the dust continuum maximum. The oxygen rich species CH_3OH and H_2CO appear to peak somewhat farther to the south. SO also is detected along the southern edge of the cloud, but seems to be associated with the outflow from KL. Only the $H^{13}CN$ image currently has sufficient sensitivity and resolution (3″ × 4″) to map substructure within CS1; the other images were made with natural weighting in order to enhance the signal to noise, and resulted in synthesized beam sizes 5″ × 7″ for CH_3CN, CH_3OH and HC_3N, and 7″ × 12″ for DCN and H_2CO.

Spectral lines observed toward the northern condensation have LSR velocities of 10.5 km s^{-1} and FWHM linewidths of about 1.5 km s^{-1}. Figure 7 shows spectra at the peak of the dust emission denoted position "A" in Figure 15. The intensity ratio of the three hyperfine components in $H^{13}CN$ is close to 5:3:1 expected for optically thin emission. An optical depth of about 0.5 for the main hyperfine line is obtained from its 4.1:1 ratio with the weakest hyperfine component. Spectra of DCN and CH_3CN at the northern cloud have been discussed previously by Mangum, Plambeck & Wootten (1991) and Wilner, Wright & Plambeck (1994).

4.2.1. Temperature

The relative intensities of the K components of the CH_3CN J=5–4 transition, with upper state energy levels from 13 K to 128 K, provide an estimate of the gas kinetic temperature in the northern cloud. Since CH_3CN is a symmetric top, with no dipole moment perpendicular to the molecular axis, radiative transitions do not change the angular momentum projected along this axis, labeled by quantum number K. Therefore, the relative populations of the different K-ladders are determined solely by collisions. Provided that the collision rate is sufficient to thermalize the rotational levels within each K-ladder, and that all transitions are optically thin, the gas kinetic temperature is just equal to the CH_3CN rotational excitation temperature. From the BIMA data, Wilner, Wright & Plambeck (1994) found that the best fit CH_3CN rotational temperature toward the northern condensation was 64 K; the $\pm 2\sigma$ range was 52–83 K.

If the collision rate is insufficient to fully thermalize the CH_3CN rotational ladders, then the simple rotational temperature overestimates the gas kinetic temperature (Loren & Mundy 1984); this occurs because levels of a given J are closer to the bottom of their K ladders, and hence have higher population, as K increases. From statistical equilibrium calculations, Wilner, Wright & Plambeck (1994) found that the J=5–4 transitions were well thermalized for a hydrogen density of 10^6 cm^{-3}, comparable to that expected for the northern cloud (see §4.2.2). For densities of 10^5 cm^{-3}, the statistical equilibrium calculations indicate the gas kinetic temperature is a little lower, about 55 K.

The CH_3CN temperature agrees well with the value of 49.3 ± 0.8 K derived from a 29″ resolution map of the J=5–4 transition of CH_3CCH (Wang et al. 1993) CH_3CCH is a symmetric top like CH_3CN, but its dipole moment is lower, 0.78 Debye as compared to 3.9 Debye for CH_3CN. Hence it is thermalized at lower hydrogen densities, $\sim 10^4$ cm^{-3} (Askne et al. 1984). Though the CH_3CCH result is based on lower angular resolution single dish observations, CH_3CCH shows no hot core spectral component which would contaminate the derived temperature.

4.2.2. Density

The detection of the J=9–8 transition of HC_3N in emission toward the northern cloud implies that the molecular hydrogen density is greater than the critical density for collisional excitation for this transition, about 10^6 cm^{-3}. Radiative trapping could lower the required density if the HC_3N line were optically thick, but this is unlikely: the peak HC_3N brightness temperature is only 26 K, while the gas kinetic temperature estimated above is ≥ 50 K. For the CS1 physical conditions, LVG calculations confirm that the optical depth in the HC_3N J=9–8 line becomes significant only if the HC_3N column density exceeds 10^{15} cm^2.

Mangum et al. (1993) also infer a density of 10^6 cm^{-3} from BIMA maps of the H_2CO $5_{1,4}$–$5_{5,0}$ line and VLA maps of the $1_{1,0}$–$1_{1,1}$ and $2_{1,1}$–$2_{1,2}$ lines, which peak toward the southern edge of the cloud. Finally, a density of 10^6 cm^{-3} is consistent with that derived from the dust continuum observations of CS1 (Wright et al. 1992).

4.2.3. Interaction with the KL Outflow

Mundy et al. (1988) argue that condensations CS1–CS4 are physically close together, most probably within 0.3–0.4 pc of one another. The high resolution maps provide several pieces of evidence that the outflow from KL impacts the southwest edge of the CS1 condensation. Some of this evidence is shown in Figure 8. The 450 micron dust continuum is shaded in each panel. The J=9–8 HC_3N line, with upper level just 20 K above the ground state, is well correlated with the

CS1 dust peak, while the 5_3–4_3 CH_3CN line (E_u/k = 78 K) and the 8_0–7_1 A^+ CH_3OH line (E_u/k = 84 K) peaks are offset to the southwest, suggesting that the gas kinetic temperature increases toward IRc2. An excitation gradient to the southwest is also visible H_2CO (Mangum et al. 1993). SO emission and a cluster of H_2O masers (Genzel et al. 1981), both indicative of shocks, are offset still farther to the southwest. SO and SO_2 line profiles at the edge of CS1 are double-peaked, perhaps indicating that the KL outflow has flowed around both the front and back of CS1. Taken together, these clues suggest that the outflow from the IRc2 region is colliding with the dense gas at the north cloud position.

It is not clear whether the northern cloud is maintained at a temperature of 50 K by radiation and shocks from IRc2 and from the Orion A HII region, or whether it contains embedded luminosity sources. Garay, Moran, and Reid (1987) found no compact continuum sources toward the northern cloud with the VLA, to a limit of 4 mJy. With $3'' \times 2''$ resolution, Murata et al. (1992) resolved the 98 GHz dust emission into 3 clumps, CntE, CntF, and CntG. With still higher resolution, $1.7'' \times 0.8''$, Plambeck et al. (1995) found a 10 mJy source coincident with CntF, suggesting that this source is associated with an exceptionally compact dust condensation. Weak line wings may be present on the $H^{13}CN$ and HC_3N spectra in Figure 7, possibly indicating the presence of an outflow or outflows from young stars; these wings might also originate from interactions with the IRc2 outflow, however.

4.3. Hot Core

Figure 2 compares maps of 12 spectral lines averaged over the velocity range $2.5 < V_{LSR} < 7.5$ km s^{-1}, a range characteristic of the hot core. Although for many molecules the hot core spectral component has a linewidth larger than 5 km s^{-1}, we've chosen a particularly narrow range in an attempt to avoid contamination from the compact ridge, which peaks at 7–9 km s^{-1}. In most cases hot core emission peaks to the east or southeast of source I. The exceptions are SiO, for which the emission peak is coincident with source I; and CH_3OH, HDO, and OCS, which are strongest south or southwest of source I. Since the latter 3 species are particularly abundant in the compact ridge, the southwestern extension is quite likely due to contamination from compact ridge gas.

Higher spatial resolution maps of the hot core are shown in Figure 9. Panel (a) is a $1''.7 \times 0''.8$ image of the 86 GHz dust continuum emission. It is identical to the map shown in Figure 2(b) of Plambeck et al. (1995), except that 34 and 84 mJy point sources at the positions of source I and BN – attributable to free-free emission from ionized circumstellar shells – were removed from the u, v data. This map is insensitive to structures $\gtrsim 8''$ in diameter, so that only the brightest clumps in the hot core are visible. The integrated flux density is 0.14 Jy, less than half the 0.41 Jy flux density found by Wright et al. (1992) for the hot core. Panel (d) overlays the v=0 J=2–1 SiO image from Figure 2(a) of Wright et al. (1995) on the dust continuum map. The SiO emission is integrated over a 30 km s^{-1} velocity range and has been restored with an $0''.5$ beam. The SiO "hourglass" is centered on source I, not the dust continuum clump. SiO brightness temperatures are as high as 3000 K, probably indicating that the line is a weak maser (Wright et al. 1995). Finally, panels (b) and (c) show $1''.7 \times 0''.8$ resolution $HC^{15}N$ and NH_2D maps which were obtained simultaneously with the 86 GHz continuum data. Each of these maps covers a 10 km s^{-1} window centered at V_{LSR} 5 km s^{-1}. The molecular line emission seems to originate from 3 main clumps spaced at about $2''$ (1000 AU) intervals. The molecular line peaks are *not* perfectly coincident with the dust continuum peaks; they are offset roughly $0''.5$ to the east. VLA observations of the NH_3(3,2) line with comparable angular resolution, $1''.24 \times 1''.20$, reveal 11 clumps with sizes $1''$–$2''$ and line widths 1–3 km s^{-1} (Migenes et al. 1989). The line widths are much lower than the overall velocity dispersion of 5–10 km s^{-1} that apparently arises from the relative motion of the individual clumps.

Figure 10 overlays a $1''.7 \times 0''.8$ image of the $H^{13}CN$ emission, integrated over the velocity range $9 < V_{LSR} < 11$ km s^{-1} to emphasize ridge gas and the western clump as well as the hot core, on the $\sim 0''.5$ resolution 3.8 micron image of this region obtained by Dougados et al. (1993). The three clumps evident in the $HC^{15}N$ image are apparent here. The infrared and molecular peaks are anticorrelated, suggesting that foreground extinction plays an important role in shaping the infrared map.

The small projected separation between the hot core and source I suggests that they are physically close. Probably they are linked kinematically as well, since the LSR velocity of source I, estimated from the midpoint of the v=1 J=2–1 SiO maser, is 5 km s^{-1}, the same as the hot core. The bulk of the hot core gas has too high a velocity dispersion and lies too far from source I to be gravitationally bound to it, but this may not be true of the dense clumps closest to the star. The mass of source I could be as large as 25 $M_\odot$ if it provides most of the 10^5 $L_\odot$ luminosity of the Kleinmann-Low Nebula; in that case the escape speed 1000 AU ($2''$) from the star is 5 km s^{-1}, comparable with the HWHM of the molecular lines.

4.3.1. Temperature

Computation of the hot core temperature based on single dish spectra is complicated by the presence of multiple velocity components in the spectra (Loren, Mundy & Erickson 1981; Loren & Mundy 1984; Andersson, Askne & Hjalmarson 1984; Sutton et al. 1986). From the aperture synthesis maps, we can generate spectra with a narrow beamwidth, and Wilner, Wright & Plambeck (1994) show CH_3CN spectra and Gaussian fits obtained towards the northern cloud, the hot core and the southern extension of the ridge.

The gas kinetic temperature in the hot core can be estimated from the CH_3CN data using the methods outlined in §4.2.1; both the rotation diagram and LVG models give T $\gtrsim$ 250 K (Wilner et al. 1994). The J=5–4 transition we observed is not well-suited for measuring the temperature of such a warm region, however. The problem is twofold: (1) the K=4 transition, the highest excitation transition observed, lies only 128 K above the ground state; (2) the broad linewidths toward the hot core cause the K=0 and 1 components, and to some extent the K=2 component, to be severely blended.

A better estimate of the hot core temperature may be obtained by comparing the intensities of the HC_3N J=9–8 transitions in the ground and ν_7 vibrational states. These HC_3N lines are pure rotational transitions, with identical A coefficients. If both lines are optically thin, the HC_3N vibrational excitation temperature T_{ex} is defined by

$$\left(\frac{T_b(vib)}{T_b(gnd)}\right) = \exp[-(E_{vib} - E_{gnd})/kT_{ex}]$$

where $T_b(vib)$ and $T_b(gnd)$ are the brightness temperatures of the the vibrational and ground state transitions and $(E_{vib} - E_{gnd})/k$ = 320 K, well matched to the temperature of the hot core. Goldsmith et al. (1982) have shown that the vibrationally excited HC_3N lines are almost certainly excited by infrared photons, not by collisions. Because these photons are well-coupled to the dust temperature, $T_{ex} \sim T_{dust}$. Multi-transition observations of HDO, CH_3CN, HC_3N show that the densities within the hot core approach 10^7 cm^{-3} (Blake et al. 1987), so the the gas kinetic temperature is likely almost equal to the dust temperature as well.

As shown in Figure 2, both the ground and excited vibrational state HC_3N transitions peak $1''$ to $2''$ southeast of source I. We estimated the excitation temperature from the ratio of the integrated intensities in a 10 km s^{-1} window centered at 5 km s^{-1}. We averaged together the intensities of the two ν_7 transitions we observed, at 82.082 and 82.200 GHz, after carefully subtracting the dust continuum, as described in §3.5. Because the ν_7 emission is spatially confined to the hot core region, while the ground vibrational state emission is much more extended, the derived excitation temperature is a function of angular resolution. With uniform weighting of the u, v data, the synthesized beam is $3\farcs7\times3\farcs2$, and the peak excitation temperature is 334 K; the $\pm1\sigma$ uncertainties give a kinetic temperature range 271 to 413 K. With natural weighting of the data, the beam is $6\farcs4\times5\farcs2$, and the peak excitation temperature is 230±15 K. Convolved with $10''$, $20''$ and $50''$ beams, we get T_{ex} = 201±10, 170±8 and 130±5 K respectively; the latter value is in good agreement with that derived by Goldsmith et al. (1982) from observations at the same resolution with the 14 meter FCRAO antenna.

Is the hot core heated externally by radiation from source I, or does it contain an embedded source of luminosity? There is some indication from the $3\farcs7\times3\farcs2$ resolution data that the HC_3N vibrational excitation temperature is greater toward source I than toward the dust continuum peak. Although this result tends to support the external heating hypothesis, much higher signal to noise data are required to confirm it.

4.3.2. Deuterated species

Both HDO and DCN are detected toward the hot core. Plambeck & Wright (1987) and Walmsley et al. (1987) find that the HDO/H_2O abundance ratio is $\sim 10^{-3}$, much larger than the cosmic D/H ratio of 10^{-5}. Deuterium enrichment by means of chemical fractionation is expected in cold (T $\lesssim$ 30 K) clouds, but not in a region as warm as the hot core. Thus, Plambeck & Wright (1987) argued that the HDO detected toward the hot core is largely fossil water, frozen onto dust grains at an earlier epoch when the cloud was much colder, and now liberated as a newly formed star or stars evaporate the grain mantles. Detection of HDO in several other "hot core" sources in G34.3+0.2, W51, Sgr B2, W3(OH) and NGC7538-IRS1 (Jacq et al. 1990) shows that the HDO/H_2O abundance ratio in Galactic hot cores is typically high, 3–6$\times 10^{-4}$, consistent with grain mantle evaporation.

The DCN/HCN abundance ratio is similarly enhanced. The HCN abundance is difficult to determine directly because of the high opacity of the HCN line, so we use the $H^{13}CN$ isotope. At $5'' \times 7''$ resolution we find a $DCN/H^{13}CN$ ratio of 0.3 at the hot core position and velocity (see Table 4); if the $HCN/H^{13}CN$ ratio is 40 (Blake et al. 1987), the DCN/HCN ratio is 7.5×10^{-3}. This agrees well with the DCN/HCN ratio of 5×10^{-3} estimated for the hot core by Mangum, Plambeck, & Wootten (1991), who used single dish $H^{13}CN$ and $HC^{15}N$ data to estimate the HCN column density. Again, such a high DCN/HCN ratio is indicative of grain mantle evaporation.

4.4. Compact Ridge

Johansson et al. (1984) were the first to point out the existence of the compact ridge emission component at LSR velocity 8 km s^{-1}. This component is particularly prominent in oxygen-rich molecules such as CH_3OH, H_2CO, HDO, and SO_2. Figure 3 compares maps of 12 species over the velocity range 7 to 9 km s^{-1}. Although emission from the hot core clump contaminates these maps, the compact ridge is evident in the SO_2, H_2CO, CH_3OH, and HDO maps as a long "streamer" extending southeast of the hot core.

The CH_3CN lines are weak toward the compact ridge, so we are unable to deduce the compact ridge temperature from CH_3CN data. Rotational temperatures derived from CH_3OH and other molecules are typically 90 – 150 K (Blake et al. 1987; Menten et al. 1988; Sutton & Herbst 1988). Densities of at least 10^6 cm^{-3} are required to explain the H_2CO emission detected by Johnston et al. (1983).

The morphology of the compact ridge, as well as its close association with the hot core, led Plambeck & Wright (1987) to speculate that it is a zone where material ablated from the hot core clump streams outward into the surrounding molecular gas. Such an interpretation is consistent with the chemical models of Blake et al. (1987), who proposed that a water-rich outflow from the IRc2 region led to the formation of complex oxygen-rich molecules in the compact ridge.

Subsequent chemical modelling by Millar, Herbst, & Charnley (1991) indicated that injection of water failed to account for the large abundances of CH_3OH, $HCOOCH_3$, and CH_3OCH_3 in the compact ridge; direct injection of CH_3OH was more successful. Methanol is particularly abundant in the region between IRc4 and IRc5, the so-called "methanol emission core" of Menten et al. (1988). Mauersberger et al. (1988) detected 8 transitions of CH_3OD from Orion which most likely originate from the same region. They estimate that the CH_3OD/CH_3OH abundance ratio is 0.01 to 0.06. Following the same arguments given in section 4.3.2, they argue that much of the methanol has been evaporated from grain surfaces.

If both water and methanol are released from grain mantles, then it is surprising that the CH_3OH and HDO emission regions are not better correlated. This poor correlation is shown clearly in Figure 3 of Plambeck & Wright (1988): HDO emission peaks most strongly toward the hot core, while the CH_3OH peak is offset about $5''$ to the southwest. A possible explanation is that methanol is released from the grain mantles at a lower temperature than water. Blake et al. (1991) performed laboratory experiments which show that amorphous mixtures of water and methanol ices convert spontaneously to a type II clathrate structure at about 120 K. The open lattice structure of the clathrate can accommodate a 7% concentration of large molecules such as CH_3OH. Sandford & Allamandola (1993) argue that any excess methanol will be released into the gas phase immediately following the formation of the clathrate, while water and other smaller molecules will remain trapped inside. This preferential release of methanol at a temperature of 120 K provides an possible explanation for its enhanced abundance in the compact ridge.

4.5. Plateau

The "plateau" component is the source of the broad line wings on molecular spectra. It consists of gas flowing outward from KL. Sometimes the plateau is further broken down into low-velocity and high-velocity outflows (e.g., Genzel & Stutzki 1989). The low velocity outflow consists of gas moving at velocities less than about 20 km s^{-1} from the ambient cloud velocity of 9 km s^{-1}; it extends along the molecular ridge. The high velocity outflow consists of faster-moving gas; it extends perpendicular to the ridge. In our view both low and high velocity outflows are manifestations of a single poorly-collimated outflow from source I.

4.5.1. Kinematics

SO and SO_2 are particularly good tracers of the low velocity outflow. Based on early maps with $6''$ resolution, Plambeck et al. (1982) argued that SO emission originated from a ring, or "doughnut", of gas expanding outward from IRc2. The newer SO and SO_2 maps, shown in Figure 11, strongly support this interpretation, although perhaps the term "pretzel" would be more apt than "doughnut." The ring is particularly clear in the 12 km s^{-1} maps. Note that the “low velocity” water masers, expanding outward from KL at about 18 km s^{-1} (Genzel et al. 1981), are well correlated with the outer edge of the ring. At 2 and 7 km s^{-1} SO and SO_2 emission originates primarily from the southeast side of the ring, while at 17 km s^{-1} the emission is strongest to the northwest.

The velocity shift from southeast to northwest is clearly apparent in the position velocity diagram in Figure 12, a cut through the SO map at position angle 135°. Emission from the hot core clump, a few arcseconds southeast of IRc2 (positive offset in the Figure), dominates the emission at 5 km s^{-1}. To the northwest, both red and blue shifted emission are visible with center of symmetry near 5 km s^{-1}. This velocity coincides with the center velocity of the SiO emission and the hot core clump, not the 9 km s^{-1} systemic velocity of the ridge gas, and strongly suggests source I lies at the center of the expansion.

At more extreme velocities the velocity pattern reverses: blueshifted emission is strongest to the west, redshifted emission to the east. Figure 13 compares maps of the high velocity SO, SO_2, SiO, HCN, and CO line wings. Although one's initial impression is of a bipolar outflow oriented east-west, this may be misleading. More careful inspection of the maps shows that there are two fingers of blueshifted gas, extending outward at position angles of roughly 20° and −90°, and two fingers of redshifted gas, at position angles of roughly 90° and −150°. Chernin & Wright (1996) argue that these emission regions represent the limb-brightened edges of broad cones of outflowing gas. Although shock-excited H_2 emission is prominent along the outflow's central axis, little molecular emission is seen along this axis, presumably because the densities there are too low to excite the lines we have observed.

The outflow center appears to lie a few arcseconds north of source I (IRc2), in agreement with lower resolution single dish maps (e.g., Wilson, Serabyn, & Henkel 1986). The existence of a 1000 AU circumstellar disk around source I (Wright et al. 1995; shown in Figures 9 and 13), elongated perpendicular to the axis of the high velocity outflow, strongly suggests, however, that source I does indeed drive the outflow. Probably the low velocity and high velocity outflows are both part of the same general expansion; low velocity emission originates where the outflow plows into the dense molecular ridge, while high velocity emission is farther from the the plane of the ridge. The northward offset of the high velocity gas can be understood if the flow to the southeast is blocked by the hot core. More detailed modelling of the outflow is described in Chernin & Wright (1996).

4.5.2. Chemical Zones

The BIMA maps indicate that there are three chemically distinct zones within the outflow: (1) an inner, SiO-rich zone closely associated with source I; (2) a shell of SO and SO_2 rich gas at the periphery of zone 1; (3) HCN and HC_3N rich gas ablated from dense clumps. Figure 4 compares high resolution SiO, SO, and $H^{13}CN$ maps which provide some of the evidence for these 3 zones. We will discuss these three regions in turn.

4.5.3. The SiO-rich zone

SiO seems to be the best probe of the innermost zone of the outflow. The powerful v=1 SiO masers occupy a 0.15″ (80 AU) diameter ring centered on source I (Plambeck et al. 1990; Wright et al. 1995), while weaker v=0 SiO masers extend over a 2″ (1000 AU) long "hourglass", also centered on source I (Wright et al. 1995). The v=1 and v=0 masers appear to delineate a flared circumstellar disk. Farther from source I the peak v=0 SiO brightness temperatures drop to about 50 K, suggesting that the emission is optically thin and thermal.

On the basis of infrared observations, Wynn-Williams et al. (1984) proposed that IRc2 is surrounded by a region of low dust opacity, a cavity with a projected diameter of 10″–20″. It is likely that the SiO-rich gas fills this cavity. Wynn-Williams et al. (1984) infer that the total H_2 column density through the cavity $\leq 10^{23}$ cm^{-2}. The SiO integrated intensity 5″ from IRc2 (safely away from the maser emission region) is roughly 1000 K-km s^{-1}; using the conversion factors given in Table 3, and assuming kinetic temperatures in the range 100–300 K, we find a total SiO column density of $1 - 3 \times 10^{16}$. Thus, the SiO fractional abundance N(SiO)/N(H_2) inside the cavity is $\sim 2 \times 10^{-7}$. While this is many orders of magnitude greater than typical dark cloud SiO abundances of $< 10^{-11}$ (Ziurys, Friburg, & Irvine 1989), it requires only that about 1% of the interstellar silicon in the cavity be in the form of SiO.

Why is the SiO abundance so high inside the infrared cavity? Chemical models show that SiO forms readily via a variety of gas phase chemical pathways (Herbst et al. 1989). Its abundance is low in most molecular clouds because virtually all the silicon has been depleted onto dust grains. The enhanced SiO abundance within the cavity indicates that additional silicon has been released into the gas phase, either directly by a protostellar wind (Glassgold, Mamon, & Huggins 1991), or by destruction of dust grains (Martin-Pintado, Bachiller, & Fuente 1992). Far infrared observations of the 35 micron fine structure line of Si^+ (Haas, Hollenbach, & Erickson 1991) provide additional evidence that the silicon abundance is enhanced near IRc2.

Most of the silicon in dust grains is expected to be bound into the refractory grain cores. Rather fast shocks, $\gtrsim 40$ km s^{-1}, are required to break up these cores (Seab & Shull 1983). Herbst et al. (1989) raise the possibility that silicon may also be trapped in the icy grain mantles, where it can be released merely by heating. This possibility appears to be ruled out by the Orion data, however, since it would predict high SiO abundances in the hot core and compact ridge, which are not observed.

It is uncertain whether shocks release silicon (or SiO) from dust grains throughout the infrared cavity, or whether the bulk of the SiO forms in the immediate vicinity of source I, perhaps by ablation of dust grains in its circumstellar disk, then is carried outward into the cavity. Martin-Pintado et al. (1992) favor the first possiblity, on the grounds that SiO molecules in the outflow would freeze back onto dust grains on timescales of less than 100 years; this would limit the radius of the SiO-rich zone to a few $\times 10^{16}$ cm, smaller by a factor of a few than the observed radius.

4.5.4. The SO and SO_2-Rich Ring

The $1.7'' \times 0.8''$ maps in Figure 4 indicate that a clumpy ring of SO emission surrounds the SiO-rich zone. Since the temperatures and densities required to excite the SO line do not differ substantially from those required to excite SiO or HC_3N, the ring presumably marks a region of enhanced SO chemical abundance. The lower resolution maps in Figure 11 show that SO_2 also is enhanced in this ring; SO and SO_2 have very similar distributions.

Evidently the SO-rich zone traces out a thin shell on the periphery of the infrared cavity. The data in Appendix A indicate that SO and SO_2 have comparable abundances in this shell. Ion-molecule chemistry (Herbst & Leung 1989) predicts an SO_2/SO ratio ~ 1 but offers no explanation of the shell structure or the high SO and SO_2 fractional abundances of 10^{-7} to 10^{-6} which are observed. Since this is the zone where the outflow from KL impinges on denser clumps in the ambient molecular ridge, it is tempting to attribute the enhanced SO abundance to shock chemistry.

Several studies have modelled the chemistry of sulfur-bearing molecules behind shocks propagating into dense molecular gas (Hartquist, Oppenheimer, & Dalgarno 1980; Mitchell 1984; Leen & Graff 1988; Neufeld & Dalgarno 1989; Pineau des Forêts et al. 1993). Both dissociative J-shock and non-dissociative C-shock models have been considered. In a J-shock (Neufeld & Dalgarno, 1989; Hollenbach & McKee 1989), the gas temperature and pressure change abruptly, and molecules are dissociated by uv radiation. Molecules re-form in the cooling gas behind the shock. In a C-shock (< 50 km s^{-1}) the gas is heated by collisions between ionized and neutral gas. A high magnetic field and low ionization fraction is required, and the heating is dispersed though a larger column of gas. Both types of shock may occur when a wind plows into dense clumps. Smith (1991) shows that neither planar, nor spherical J-shocks form a self consistent explanation of the observed H_2, CO, OI and OH line emission in Orion, whereas bow shocks are able to provide a range of shock parameters needed to explain the high temperature H_2 emission and the slower $<$ 20–25 km s^{-1} shocks needed to explain the CO line emission.

Generally the chemical models assume that sulfur is primarily in atomic form in the preshock gas, and find that the SO and/or SO_2 abundances are enhanced behind the shock. The exception is the Leen & Graff (1988) study, which has most of the preshock sulfur in SO and SO_2, and finds a slight decrease in their abundances through the shock. The models do differ widely in their predictions of the SO/SO_2 ratio in the postshock gas. Both the nondissociative shock model of Hartquist et al. (1980) and the dissociative shock model of Neufeld & Dalgarno predict an SO/SO_2 ratio $\sim 10^3$ to 10^4, while the more recent nondissociative model of Pineau des Forêts et al. (1993) finds SO/$SO_2 \ll 1$. In this last model, the SO abundance is higher in a thin layer immediately behind the shock, but the reaction SO + OH $\rightarrow$ SO_2 + H converts most of the SO to SO_2 in a 10^{17} to 10^{18} cm thick layer behind the shock. Melnick et al. (1990) find that the far infrared OH emission from Orion is consistent with a 38 km s^{-1} C-shock; their data suggests that a high abundance of OH is available to drive ion-molecule chemistry in the shocked region.

Further work is needed to see if the SO_2/SO ratio ~ 1 which we observe is compatible with such a model.

4.5.5. Ablation from Dense Clumps

Figure 4 shows that HCN is well correlated with neither the SiO nor the SO distributions. HCN and HC_3N appear to be associated with dense clumps (as evidenced by good correlation with continuum, see Figures 1–3) but do not show a complete ring like SO and are not associated with the source I disk like SiO.

HC_3N is well correlated with HCN, but both seem poorly correlated with SO when examining narrow velocity channels – see, for example, Figure 14, which compares HC_3N and SO maps in 1 km s^{-1} wide intervals. We suspect the high velocity HC_3N and HCN line wings are attributable to ablation from preexisting dense clumps. Probably these species are not created chemically (perhaps they are destroyed) in oxygen-rich envelopes of the clumps where SO emission is strongest.

5. Summary

We have presented images of the Orion-KL region at $1'' - 6''$ resolution in 28 transitions of 16 molecular species. The maps are available in FITS format from the NCSA digital image library via URL *http://imagelib.ncsa.uiuc.edu/imagelib*. A comparison of the maps leads to the following principal conclusions:

1. There are two main concentrations of molecular gas within the $2'$ field of view. The chemistry and kinematics of these two regions are strikingly different. The southern concentration corresponds to the Kleinmann Low Nebula, a region of intense star formation activity; it contains embedded infrared sources, powerful SiO and H_2O masers, and a high velocity bipolar outflow. The northern concentration corresponds to the CS1 dust continuum peak; it has narrow linewidths and shows little indication of active star formation.

2. Both molecular concentrations are embedded within a molecular ridge which extends from northeast to southwest. The velocity of the ridge gas changes discontinuously at the Kleinmann Low Nebula. Approaching from the south, the velocity decreases from 8 to about 6 km s^{-1}; from the north, it increases from 10 to about 11 km s^{-1}. This velocity divergence may be interpreted either as differential rotation around KL, or as acceleration of ambient gas by the outflow from KL. Because the maps show numerous signs of interaction between the KL outflow and the southern edge of the CS1 condensation (heating, water masers, SO emission characteristic of shocked gas), we lean toward the second interpretation. This implies that the KL region lies somewhat in front of the CS1 cloud.

3. The temperature of the northern condensation, CS1, is inferred to be 55-65 K from CH_3CN data. CH_3OH and CH_3CN K=3 emission along the southern edge of the cloud suggests that this region is warmer.

4. At $1''$ resolution, the hot core appears as a chain of dense clumps in continuum, $H^{13}CN$, $HC^{15}N$, and NH_2D maps. This chain is elongated at position angle $30°$ and is centered $\sim 1''$ east of continuum source I. These clumps are anticorrelated with 3.8 micron infrared peaks, suggesting that foreground extinction plays an important role in shaping the infrared map. The HC_3N vibrational excitation temperature is estimated to be 335 K toward the hot core.

5. The high abundance of HDO, DCN, and other deuterated species in the hot core suggests that icy grain mantles have recently evaporated in these regions. CH_3OH, another likely constituent of the grain mantles, is more abundant in the compact ridge, about $5''$ southeast of the hot core, indicating that it is released from the grain mantles at a lower temperature than H_2O. The selective evaporation of methanol from clathrate structures in mixed molecular ices at a temperature of about 120 K may explain this phenomenon, and account for the peculiar chemistry of the compact ridge.

6. A bipolar outflow from KL is responsible for the "plateau" emission component. Radio continuum source I, associated with the IRc2 infrared peak, is the most plausible source of the outflow. The high resolution v=0 SiO map appears to define a 1000 AU diameter flared disk approximately perpendicular to the high velocity outflow; regions of weak v=0 SiO maser emission lie within the disk approximately 300 AU northeast and southwest of source I. The powerful v=1 SiO masers lie in a 40–80 AU diameter annulus at the center of this disk.

7. High velocity molecular gas associated with the outflow is not confined to narrow jets. Rather, maps of the line wings show broad, bowl-shaped regions which may represent the limb-brightened edges of broad cones of outflowing gas. The axis of these cones is northwest-southeast, approximately along the lobes of shock-excited H_2. Both red-shifted and blue-shifted outflow emission are visible to the northwest, while the outflow appears partially blocked to the southeast, at the hot core, just $\sim 2''$ from source I.

8. There appear to be 3 chemically distinct zones within the outflow. The innermost zone appears to correspond to the infrared cavity of Wynn-Williams et al. (1984); the SiO fractional abundance in this region is high, roughly 2×10^{-7}, suggesting that refractory dust grain cores are destroyed here. Surrounding the SiO-rich zone is an expanding shell prominent in SO and SO_2 emission, probably indicating the zone where the outflow from source I shocks ambient dense clumps. Finally, high velocity HCN and HC_3N emission appear to trace material ablated from dense clumps at the periphery of the cavity.

We thank the Hat Creek staff for their contributions to the development and operation of the BIMA array. This work was partially supported by NSF grant AST 93-20238 to the University of California. D.J.W. acknowledges a Center for Astrophysics postdoctoral fellowship.

A. Chemical Abundances

In this appendix, we derive column densities and fractional abundances for 14 mapped species at 9 positions in the Orion-KL region. Although different lines peak at different positions, we would like to avoid a bias toward any one particular line in selecting positions in the images at which to extract spectra. Thus, we have chosen 9 positions from the 3 millimeter dust continuum image. These positions are shown in Figure 15.

All of the spectra were obtained from images made with natural weighting of the visibilities to maximize the signal-to-noise ratio. The beam size was approximately $5'' \times 7''$ for all the transitions except for the lower frequency DCN and H_2CO lines with beam size about $7'' \times 12''$. This angular resolution clearly averages over some small scale structure, particularly in the vicinity of the hot core. Even at $5'' \times 7''$ resolution, many positions show several spectral components, and these components may show dramatic chemical differences.

In an attempt to separate the spectral components at each of the 9 positions, we used a Gaussian fitting procedure. The Gaussian components were chosen to characterize the average spectrum for the most prominent species at each position. In some cases, these fixed Gaussian components are relatively poor representations of the data; better fits could be obtained by chosing a different set of Gaussian components for each line. However, such detailed fits of multiple components for each species at each position would make difficult the comparison of relative abundances within each component. We compromised by fitting 3 Gaussian components to each spectrum: a narrow component, whose velocity and width varies, to represent the quiescent ridge, hot core, western clump, or compact ridge emission, and broad redshifted and blueshifted components, with fixed velocity and width (v=0,20 km s^{-1}, Δv=20 km s^{-1}), to represent the plateau emission. We provide some notes on the Gaussian fits at each of the 9 positions below.

We derived column densities for each species within each Gaussian component assuming optically thin LTE conditions. From the JPL spectral line catalog (Pickett, Poynter, & Cohen, 1992), a line intensity I_{ba} (300 K) was obtained for each transition:

$$I_{ba}(T) = (8\pi^3/3\mathrm{hc})\nu_{ba}\ {}^{x}S_{ba}\ \mu_x^2[e^{-E''/kT} - e^{-E'/kT}]/Q_{rs} \tag{A1}$$

where ν_{ba} is the line frequency, ${}^{x}S_{ba}$ is the line strength, μ_x is the dipole moment along the molecular axis x, E$''$ and E$'$ are the lower and upper state energies, respectively, and Q_{rs} is the rotation-spin partition function (as tabulated in the catalog). The units of $I_{ba}(T)$ are given as nm^2 MHz - the integral of the absorption cross-section across the line shape. In the Rayleigh-Jeans limit, we calculated the absorption cross-section integrated over a 1 km s^{-1} velocity interval as:

$$\sigma_{ba} = \frac{I_{ba}}{\nu_{ba}} \times 2.99792 \times 10^{-9}\ \mathrm{cm}^2. \tag{A2}$$

The inverse of σ_{ba}, the column density per unit optical depth in a 1 km s^{-1} velocity interval, was divided by the excitation temperature and listed for each species in Table 3 for temperatures from

50 to 300 K. For optically thin emission, column densities are obtained by multiplying these values by the integrated intensities as observed in units of K km s^{-1}. In most cases, the BIMA line survey set containes only a single transition of a given species, and excitation temperatures cannot be derived from the data set. Following the CH_3CN analysis of Wilner, Wright & Plambeck (1994), we adopt temperatures of 50 K for the north ridge region, 100 K for the compact ridge and outflow components, and 200 K for the hot core. The adoption of different temperatures changes the the derived column densities somewhat, an effect easily taken into account for any particular species using Table 3. Table 4 lists the column densities for each position and spectral component using the listed temperatures, and Figure 16 provides a graphical representation. The derived column densities are probably accurate to an order of magnitude.

The fractional abundance for each component may be calculated by assuming a dust temperature equal to the molecular kinetic temperature, and estimating a hydrogen column density from the optically thin 3 millimeter dust emission shown in Figure 15, using the relationship $N(H + H_2) = 1.2 \times 10^{24} \;\times\; \tau(0.4\ mm)$ (Keene, Hildebrand, and Whitcomb 1982). Following Wright etal (1992), we assumed a dust opacity spectral index β of 2.0 for the Hot Core and 1.5 for the other components. Since we cannot apportion the dust emission between the different spectral components at each position, the fractional abundances computed from the dust and molecular column density listed in Table 4 should be considered lower limits.

Below we describe some details of the Gaussian fitting procedure at each of the 9 positions.

For the North cloud (position A), a narrow component with fixed velocity and width together with a continuum level provided a good fit to all species except HCN which was observed with coarse velocity resolution. Allowing the center and width to vary we obtained center velocities from 9.9 to 10.8 km s^{-1}, widths from 0.8 to 1.7 km s^{-1}, and line integrals within 20 percent of the values obtained with a fixed center and width. There is some evidence for a shoulder on the $H^{13}CN$ and HC_3N profiles; this may indicate an outflow from an embedded source. However, there is no evidence for high velocity components at this position, and components at 20 and 0 km s^{-1} were not considered.

North Ridge interaction region (B) spectra show evidence of the outflow; we fitted 3 Gaussian components: a ridge component with center 10.4 km s^{-1} and width 1.8 km s^{-1}, and line wings which we fitted as red and blue-shifted components with centers at 20 and 0 km s^{-1} and widths 20 km s^{-1}. Allowing the width of the ridge component to vary resulted in better fits, and a transfer of integrated emission from the line wings to the ridge component, especially for the SO and SO_2 emission.

At the North Core (C), we fitted a hot core component with center 5 and width 5 km s^{-1} and high velocity components at 20 and 0 km s^{-1} as above. The line wings are poorly represented by smooth Gaussian components at this position. Several subcomponents can be identified at -5, 12, 21, 32 km s^{-1} in the SiO, SO and HC_3N spectra, perhaps evidence of discrete clumps in the outflow.

We fitted a Hot Core component (D) with center 5 and width 5 km s^{-1} and high velocity components at 20 and 0 km s^{-1} as above. For OCS and CH_3OH, the peak is closer to 8 km s^{-1}. These species are dominated by compact ridge emission, and the column densities listed in Table 4 should be regarded as upper limits. There may in fact be little or no OCS and CH_3OH emission from the dense hot core region. The SiO emission, which peaks close to IRc2, is also poorly fitted at the hot core position; the $0\farcs7\times1\farcs7$ resolution image shows that the SiO emission is clearly displaced from the hot core dust peak.

The Western Peak (E) is well fitted with a narrow component at 8 to 15 km s^{-1} with widths 8 to 12 km s^{-1} together with high velocity components at 20 and 0 km s^{-1} as above. The peak is close to 12 to 14 km s^{-1} for SiO, SO, SO_2, $H^{13}CN$, but closer to 8 km/s for OCS and CH_3OH. A relatively poor fit was obtained for CH_3OH, which is probably weakly masing close to this position.

For the South Core (F), reasonable fits were obtained with a narrow component at 7 to 9 km s^{-1} and width 2 to 5 km s^{-1} together with high velocity components at 20 and 0 km/s as above, except for SO_2 and HCN. The SO_2 shows narrower line wings than assumed in the fit, and the coarse velocity resolution of the HCN data compromises the narrow component.

Good fits were obtained in the South Ridge (G) with a narrow component at 8 to 9 km s^{-1} and fixed width 2 km s^{-1} together with the high velocity components at 20 and 0 km/s as above. The SiO line shows little evidence for the narrow component.

The Compact Ridge (H and I) is best fitted with a narrow component at 7 to 11 km s^{-1} and width 2 to 4 km s^{-1} together with the high velocity components at 20 and 0 km/s as above. The SiO, SO and SO_2 do not show much evidence for the narrow component. SO_2 emission extends further to the east than SO emission.

Table 1. Molecular lines mapped toward Orion-KL with the BIMA array.

molecule	transition	ν (GHz)	E_u/k	beam ($''$)	Δv (km s^{-1})	dates.	ref.
H_2CO	$5_{1,4}$–$5_{1,5}$	72.40909	65.9	7.4×7.9	0.3	88dec–89oct	10
DCN	J=1–0, F=1–1	72.41351	3.5	7.4×7.9	0.3	88dec–89oct	11
	J=1–0, F=2–1	72.41493					
	J=1–0, F=0–1	72.41703					
HDO	$1_{1,0}$–$1_{1,1}$	80.57828	46.8	3.3×3.5	0.6	85dec–86nov	2
CH_3CH_2CN	$9_{6,3}$–$8_{6,2}$ + $9_{6,4}$–$8_{6,3}$	80.60213	37.2	3.3×4.2	0.6	85dec–86nov	1
	$9_{5,5}$–$8_{5,4}$ + $9_{5,4}$–$8_{5,3}$	80.60458					
	$9_{7,3}$–$8_{7,2}$ + $9_{7,2}$–$8_{7,1}$	80.60621					
	$9_{4,6}$–$8_{4,5}$ + $9_{4,5}$–$8_{4,4}$	80.61946					
HC_3N	J=9–8	81.88147	19.7	3.2×3.7	1.1	85oct–86jun	1
	J=9–8 ν_7 1e–1e	82.08273	340.				
	J=9–8 ν_7 1f–1f	82.20037	340.				
SO_2	$8_{1,7}$–$8_{0,8}$	83.68809	36.7	3.4×3.9	0.6	85feb–86nov	1
OCS	J=7–6	85.13911	16.4	2.8×3.4	1.1	85oct–86jun	1
^{29}SiO	v=0 J=2–1	85.75913	6.3	2.4×4.4	4.2	81oct–83may	1,9
SO	$N_J = 2_2 - 1_1$	86.09396	19.3	3.2×3.9	0.3	93nov–95jan	1,12
SiO	v=1 J=2–1 (maser)	86.24335	1770.	1.5×2.4	1.1	93nov–95jan	6,7
SiO	v=0 J=2–1	86.84700	6.3	3.1×3.9	1.1	93nov–95jan	1,8
$H^{13}CN$	J=1–0, F=1–1	86.33877	4.3	3.1×3.9	0.3	93nov–95jan	1
	J=1–0, F=2–1	86.34018					
	J=1–0, F=1–0	86.34227					
HCN	J=1–0, F=1–1	88.63042	4.3	5.6×6.0	0.9	82feb–82may	1,4
	J=1–0, F=2–1	88.63185					
	J=1–0, F=0–1	88.63394					
HCO^+	J=1–0	89.18852	4.3	16×18	4.1	81oct–82may	5
CH_3CN	J_K=5_4–4_4	91.95873	127.8	3.1×3.9	0.5	85dec–86may	1,13
	J_K=5_3–4_3	91.97113	77.6				
	J_K=5_2–4_2	91.98000	41.9				
	J_K=5_1–4_1	91.98532	20.8				
	J_K=5_1–4_1	91.98709	13.7				
CH_3OH	8_0–7_1 A^+	95.16948	83.6	3.1×3.9	0.5	85dec–86may	3
CO	J=1–0	115.27120	5.5	3.2×2.6	0.25	95feb–95may	14

References. — (1) This paper; (2) Plambeck & Wright 1987; (3) Plambeck & Wright 1988; (4) Vogel et al. 1985; (5) Vogel et al. 1984; (6) Plambeck et al. 1990; (7) Wright et al 1990; (8) Wright et al. 1983; (9) Plambeck et al. 1985; (10) Mangum et al. 1993; (11) Mangum et al. 1991; (12) Plambeck et al. 1982; (13) Wilner et al. 1994; (14) Chernin & Wright 1996.

Table 2. Orion-KL region spectral components

component	velocity range (km s^{-1})	comment
ridge	7 to 11	quiescent dense gas
compact ridge	7 to 9	material ablated from clumps
north cloud	10 to 11	condensation in ridge
hot core	2.5 to 7.5	hot dense clump in infrared cavity
western clump	10 to 14	dense clump in infrared cavity
low velocity	$8 < \|v - 9\| < 20$	low velocity outflow
high velocity	$20 < \|v - 9\|$	high velocity outflow

Table 3. Column density (cm^{-2}) per K km s^{-1} interval

line	50 K	60 K	100 K	100 K	200 K	250 K	300 K
H_2CO	2.76E+14	2.91E+14	4.08E+14	4.80E+14	8.32E+14	1.09E+15	1.37E+15
DCN	7.83E+12	9.27E+12	1.53E+13	1.82E+13	3.02E+13	3.76E+13	4.50E+13
HDO	8.35E+13	9.06E+13	1.45E+14	1.73E+14	3.19E+14	4.26E+14	5.43E+14
CH_3CH_2CN	3.59E+13	3.94E+13	5.90E+13	7.09E+13	1.27E+14	1.68E+14	2.13E+14
HC_3N	5.39E+12	6.09E+12	9.02E+12	1.05E+13	1.65E+13	2.03E+13	2.40E+13
SO_2	9.46E+13	1.11E+14	1.89E+14	2.34E+14	4.49E+14	6.07E+14	7.80E+14
OCS	1.25E+14	1.43E+14	2.17E+14	2.54E+14	4.04E+14	4.97E+14	5.91E+14
SO	9.15E+13	1.13E+14	1.68E+14	2.06E+14	3.30E+14	4.05E+14	4.85E+14
$H^{13}CN$	5.56E+12	6.57E+12	1.08E+13	1.29E+13	2.13E+13	2.65E+13	3.17E+13
SiO	5.25E+12	6.19E+12	1.00E+13	1.19E+13	1.96E+13	2.43E+13	2.91E+13
HCN	5.24E+12	6.19E+12	1.02E+13	1.21E+13	2.00E+13	2.50E+13	2.99E+13
CH_3CN	3.88E+12	4.61E+12	7.97E+12	9.86E+12	1.86E+13	2.50E+13	3.20E+13
CH_3OH	5.62E+14	5.63E+14	7.05E+14	8.10E+14	1.33E+15	1.71E+15	2.13E+15
CO	2.35E+15	2.76E+15	4.52E+15	5.36E+15	8.84E+15	1.10E+16	1.32E+16

Table 4. Calculated LTE molecular column densities for 9 positions (units 10^{16} cm^{-2}).

	v	Δv	T_k	H_2[a]	SiO	SO	SO_2	OCS	HCN	$H^{13}CN$	HC_3N	DCN	H_2CO	CH_3CN	CH_3OH	HDO	ECN
A	10.4	1.5	50.0	9.34	···	0.11	0.02	0.03	0.13	0.04	0.03	0.02	0.16	0.05	0.75	···	···
B	10.4	1.8	100.0	2.04	0.01	1.80	1.30	0.07	0.33	0.07	0.03	0.01	0.49	0.07	2.61	0.20	···
B	0.0	20.0	100.0	2.04	0.07	1.78	0.85	0.82	0.36	0.04	···	0.05	3.30	0.05	0.85	0.19	···
B	20.0	20.0	100.0	2.04	0.10	2.47	1.00	0.13	0.29	0.03	0.00	···	1.26	0.05	0.71	0.07	···
C	5.0	5.0	100.0	2.92	0.02	0.37	0.20	0.49	···	0.07	0.04	0.01	0.12	0.13	0.56	0.21	···
C	0.0	20.0	100.0	2.92	0.62	11.14	8.07	2.26	1.34	0.42	0.11	0.09	8.45	0.33	2.96	0.61	···
C	20.0	20.0	100.0	2.92	0.53	10.48	7.79	1.22	0.88	0.12	0.04	···	1.63	0.11	4.23	0.46	···
D	5.0	5.0	200.0	8.85	0.61	4.78	5.03	4.93	0.09	0.60	0.23	0.17	0.92	1.47	20.61	5.20	2.87
D	0.0	20.0	100.0	6.00	1.78	15.86	15.35	4.75	1.76	0.89	0.45	0.13	15.79	0.54	8.04	2.60	2.69
D	20.0	20.0	100.0	6.00	1.29	10.23	10.26	2.95	1.04	0.30	0.12	···	2.61	0.34	5.64	1.35	0.64
E	12.0	5.0	100.0	4.09	0.14	3.78	3.70	2.82	0.27	0.26	0.06	0.13	2.94	0.36	13.47	0.23	···
E	0.0	20.0	100.0	4.09	0.53	9.00	7.65	1.15	0.87	0.28	0.07	0.07	8.57	0.24	7.26	0.48	···
E	20.0	20.0	100.0	4.09	0.28	6.52	5.29	1.02	0.70	0.13	0.06	···	1.10	0.15	4.86	0.74	···
F	8.0	2.0	100.0	1.90	0.39	5.31	1.08	1.76	0.39	0.12	0.03	0.04	1.92	0.24	10.86	1.10	···
F	0.0	20.0	100.0	1.90	0.12	3.80	6.79	1.63	0.63	0.22	0.10	0.11	6.61	0.19	9.31	0.81	···
F	20.0	20.0	100.0	1.90	0.24	6.22	6.07	1.28	0.64	0.12	0.03	···	1.67	0.03	4.79	0.43	···
G	8.0	2.0	100.0	1.90	0.00	0.44	0.38	0.50	0.11	0.05	0.02	0.02	1.18	0.05	4.79	0.20	···
G	0.0	20.0	100.0	1.90	0.04	0.82	0.04	0.13	0.04	0.02	···	0.07	···	0.02	2.96	0.35	···
G	20.0	20.0	100.0	1.90	0.03	0.82	0.40	0.17	0.06	0.01	0.02	0.05	0.98	···	2.40	···	···
H	8.0	2.0	100.0	1.90	0.09	2.87	2.29	0.89	0.43	0.08	0.06	0.04	2.69	0.10	5.64	0.81	···
H	0.0	20.0	100.0	1.90	0.04	1.26	2.25	1.00	0.20	0.06	0.05	0.07	1.67	0.05	4.23	0.38	···
H	20.0	20.0	100.0	1.90	0.08	1.33	2.74	0.39	0.26	0.04	0.01	···	1.88	0.01	2.33	0.48	···
I	8.0	2.0	100.0	1.90	0.03	0.77	1.63	···	···	0.03	0.02	···	0.49	0.05	3.60	0.36	···
I	0.0	20.0	100.0	1.90	0.02	0.49	1.55	0.48	0.07	0.01	···	···	3.88	···	1.83	···	···
I	20.0	20.0	100.0	1.90	0.10	0.60	1.08	0.09	0.11	0.02	0.01	···	1.84	0.02	1.27	0.30	···

[a]column density of molecular hydgrogen derived from optically thin 3 mm dust emission (units 10^{23} cm^{-2}).

REFERENCES

Andersson, M., Askne, J., & Hjalmarson, Å. 1984, A&A, 136, 243

Askne, J., Hoglund, B., Hjalmarson, Å. & Irvine, W.M. 1984, A&A, 130, 311

Bastien, P., Batrla, W., Henkel, C., Pauls, T., Walmsley, C.M., & Wilson, T.L. 1985, A&A, 146 86

Becklin, E.E. & Neugebauer,G. 1967, ApJ, 147, 799

Beckwith, S., Persson, S.E., Neugebauer, G., & Becklin, E.E., 1978, ApJ, 223, 464

Blake, D., Allamandola, L., Sandford, S., & Freund, F. 1991, Science, 254, 548

Blake, G.A., Sutton, E.C., Masson, C.R., & Phillips, T.G. 1986, ApJS, 60, 357

Blake, G.A., Sutton, E.C., Masson, C.R., & Phillips, T.G. 1987, ApJ, 315 621

Brown, P.D., Charnley, S.B. & Millar, 1988, MNRAS, 231, 409

Carlstrom, J.E., Plambeck, R.L, & Thornton, D.D. 1985, URSI symposium on Millimeter & Submillimeter wave radio astronomy. p. 149

Caselli, P., Hasegawa, T. I., & Herbst, E. 1993, ApJ, 408, 548

Charnley, S.B., Tielens, A.G.G.M., & Millar, T.J., 1992, ApJ399, L71

Chernin, L.M. & Wright, M.C.H. 1996, ApJ, submitted.

Cornwell, T.J., Uson, J.M., & Haddad, N. 1992, A&A, 258, 583

Dougados, C., Lena, P., Ridgway, S.T., Christou, J.C. & Probst, R.G. 1993, ApJ, 406 112

Erickson, N.R., et al. 1982, ApJ, 261, L103

Garay, G., Moran, J.M., & Reid, M.J. 1987, ApJ, 314, 535

Goldsmith, P.F., Snell, R.L., Deguchi, S., Krotkov, R., & Linke, R.A. 1982, ApJ, 260, 147

Gezari, D.Y. 1992, ApJ, 396, L43

Genzel, R., Reid, M.J., Moran, J.M., & Downes, D. 1981, ApJ, 244, 884

Genzel, R. & Stutzki, J. 1989, ARA&A, 27, 41

Glassgold, A.E., Mamon, G.A. & Huggins, P.J., 1991, ApJ, 373, 254

Guilloteau, S., etal 1992, A&A, 262, 624

Haas, M.R., Hollenbach, D., & Erickson, E.F. 1991, ApJ, 374, 555.

Hartquist, T.W., Oppenheimer, M. & Dalgarno, A., 1980, ApJ, 236, 182

Hasegawa,T. etal., 1984, ApJ, 283, 117

Herbst, E. & Leung, C.M. 1989, ApJS, 69, 271

Herbst, E., Millar, T.J., Wlodek, S., & Bohme, D.K. 1989, A&A, 222, 205

Ho, P.T.P & Barrett, A.H., 1978, ApJ, 224, L23

Hollenbach, D. & McKee, C.F., 1989, ApJ, 342, 306

Jacq, T., Walmsley,C.M., Henkel,C., Baudry,A., Mauersberger,R., & Jewel,P.R. 1990, A&A, 228, 447

Johnston, K.J., Palmer, P., Wilson, T.L., & Bieging, J.H. 1983, ApJ, 271, L89

Johansson, L.E.B., Andersson, C., Ellder, J., Friberg, P., Hjalmarson, Hoglund, B., Irvine, W.M., Olofsson, H., & Rydbeck, G. 1984, A&A, 130, 227

Leen, T.M., & Graff, M.M. 1988, ApJ, 325, 411

Loren, R.B., Mundy, L.G. & Erickson,N.R. 1981, ApJ, 250, 573

Loren, R.B. & Mundy, L.G. 1984, ApJ, 286, 232

Mangum, J.G., Plambeck,R.L., & Wooten,A. 1991, ApJ, 369, 169

Mangum, J.G., Wooten,A., & Plambeck,R.L. 1993, ApJ, 409, 282

Martín-Pintado, J., Bachiller, R., & Fuente, A. 1992, A&A, 254, 315

Mauersberger, R., Henkel, C., Jacq, T., & Walmsley, C.M. 1988, A&A, 194, L1

Keene, J., Hildebrand, R.H. & Whitcomb, S.E., 1982, ApJ, 252, L11

Melnick, G.J., Stacey, G.J., Genzel R, Lugten, J.B. & Poglitsch, A. 1990, ApJ, 348, 161

Menten, K.M., Walmsley, C.M., Henkel, C., & Wilson, T.L. 1988, A&A, 198, 253

Menten, K.M. & Reid, M.J. 1995, ApJ, 445, L157

Millar, T.J., Herbst, E. & Charnley, S.B., 1991, 369, 147

Mitchell, G.F. 1984, ApJ, 287, 665

Moran, J.M., Garay, G., Reid, M.J., Genzel, R., Wright, M.C.H., & Plambeck 1983, ApJ, 271, L31

Morita, K.I., Hasagawa, T., Ukita, N., Okumura, K. & Ishiguro, M. 1992, PASJ, 44, 373

Migenes, V., Johnston, K.J., Pauls, T.A., & Wilson, T.L. 1989, ApJ, 347, 294

Mundy, L.G., Scoville, N.Z., Baath, L.B., Masson, C.R., & Woody, D.P. 1986, ApJ, 304, L51

Mundy, L.G., Cornwell, T.J., Masson, C.R., Scoville, N.Z., Baath, L.B., & Johansson, L.E.B. 1988, ApJ, 325, 382

Murata, Y., Kawabe, R., Ishiguro, M., Morita, K.-I., Hasegawa,T., & Hayashi, M. 1992, PASJ, 44, 381

Neufeld, D.A. & Dalgarno,A. 1989, ApJ, 340, 869

Olofsson, H., Hjalmarson, Å., & Rydbeck, O.E.H. 1981, A&A, 100, L30

Pickett, H.M., Poynter, R.L., & Cohen, E.A. 1992, JPL Publication 80-23

Pineau des Forêts, G., Roueff, E., Schilke, P., & Flower, D.R. 1991, MNRAS, 262, 915

Plambeck, R.L. & Wright, M.C.H., 1987, ApJ, 317, L101

Plambeck, R.L. & Wright, M.C.H. 1988, ApJ, 330, L61

Plambeck, R.L. etal, 1982, ApJ, 259, 617

Plambeck, R., Thatte, N., & Sykes, P. 1993, Proc. 7th International Cryocooler Conf., Phillips Laboratory report PL-CP-93-1001, Kirtland AFB, NM, p.401

Plambeck, R.L., Wright, M.C.H., Mundy, L.G. & Looney, L.W., 1995, ApJ, 455, 189

Plambeck, R.L. Wright, M.C.H. & Carlstrom, J.E. 1990, ApJ, 348, L65

Sandford, S.A. & Allamandola, L.J. 1993, ApJ, 417, 815

Seab, C.G., & Shull, J.M. 1983, ApJ, 275, 652

Smith, M.D. 1991, MNRAS, 253, 175

Sutton, E.C., Blake, G.A., Masson, C.R., & Phillips, T.G. 1985, ApJS, 58, 341

Sutton, E.C., Blake, G.A., Genzel, R., Masson, C.R., & Phillips, T.G. 1986, ApJ, 311, 921

Sutton, E.C., & Herbst, E. 1988, ApJ, 333, 359

Sutton, E.C., Peng, R., Danchi, W.C. etal. 1995, ApJS, 97, 455

Ulich, B.L. 1981, AJ, 86, 1619

Ulich, B.L. & Haas, R.W. 1976, ApJS, 30, 247

Urry, W.L., Thornton, D.D., & Hudson,J.A., 1985, PASP, 97, 745

Vogel, S.N., Wright, M.C.H., Plambeck, R.L, & Welch, W.J., 1984, Ap.J. 283, 655

Vogel, S.N., Bieging, J.H., Plambeck, R.L., Welch, W.J., & Wright, M.C.H., 1985, Ap.J., 296, 600

Walmsley, C.M., Hermsen,W., Henkel,C., Mauersberger,R., & Wilson, T.L. 1987, A&A, 172, 311

Wang, T.Y., Wouterloot, J.G.A. & Wilson, T.L. 1993, A&A, 277, 205

Welch, W.J., Wright, M.C.H., Plambeck, R.L., Bieging, J.H., & Baud, B., 1981, ApJ, 245, L87

Welch, W.J., et al. 1996, PASP, 108, 93

Wilson, T.L., Serabyn, E., Henkel, C., & Walmsley, C.M. 1986, A&A, 158, L1

Wilner, D.J., Wright, M.C.H. & Plambeck, R.L. 1994, ApJ, 422, 642

Womack, M., Ziurys, L.M. & Sage, L.J., 1993, ApJ, 406, L29

Wright, M.C.H. & Plambeck, R.L. 1983, ApJ, 267 L115

Wright, M.C.H., Plambeck, R.L., Vogel, S.N., Ho, P.T.P., & Welch, W.J. 1983, ApJ 267, L41

Wright, M.C.H., Carlstrom, J.E.,Plambeck, R.L., & Welch,W.J. 1990, AJ, 99, 1299

Wright, M.C.H. & Sault, R.J., 1991, IAU Coll 131, ASP conference series 19, 276. T.J.Cornwell & R.A.Perley (eds).

Wright, M.C.H., Sandell, D.J., Wilner, D., & Plambeck,R.L. 1992, ApJ, 393, 225

Wright, M.C.H., Plambeck, R.L., Mundy, L.G. & Looney, L.W., 1995, ApJ, 455, 185

Wynn-Williams, C.G., Genzel,G., Becklin,E.E., & Downes,D. 1984, ApJ, 281, 172

Ziurys, L.M., Friberg, P. & Irvine, W.M., 1989, ApJ, 343, 201

This preprint was prepared with the AAS LaTeX macros v4.0.

Fig. 1.— Ridge tracers in Orion: 3 millimeter dust continuum and molecular line emission mapped in the velocity range $7 < V_{LSR} < 11$ km s^{-1}. The contour intervals and beam sizes are: SiO (40 K; $3''.9\times3''.1$), SO (10 K; $3''.9\times3''.2$), SO_2 (10 K; $3''.9\times3''.4$), OCS (5 K; $6''.7\times4''.9$), $H^{13}CN$ (5, 10 K and then from 15 K at intervals 10 K; $3''.9\times3''.1$), HC_3N (4 K; $6''.4\times5''.2$), HCN (5, 10 K and at intervals 10 K; $6''.0\times5''.6$), CH_3CH_2CN(2.3, and then from 4.7 K at 4.7 K intervals; $7''.7\times5''.2$), CH_3CN(3.9 K, and then from 7.8 K at 7.8 K intervals; $7''.3\times5''.1$), CH_3OH(3.9 K, and then from 11.6 K at 7.7 K intervals; $7''.1\times4''.9$), HDO(2.4 K and then from 4.7 K at 4.7 K intervals; beam $7''.7\times5''.2$), dust (0.26 K; $7''.0\times5''.1$). The positions of radio sources BN and I are marked by filled squares.

Fig. 2.— Maps of molecular line emission from Orion over the velocity range $2.5 < V_{LSR} < 7.5$ km s^{-1}, characteristic of the hot core. The contour interval is 2 K for vibrationally excited HC_3N (the average of the two ν_7 lines); 5 K for HC_3N and DCN; 10 K for CH_3CN, CH_3OH, HDO, SO, CH_3CH_2CN, and $H^{13}CN$; 15 K for SO_2 and OCS; and 40 K for SiO. The positions of radio sources BN and I are marked by filled squares.

Fig. 3.— Maps of molecular line emission from Orion over the velocity range $7 < V_{LSR} < 9$ km s^{-1}, characteristic of the compact ridge. The contour interval is 10 K for $H^{13}CN$, CH_3CN, CH_3OH, and SO (which has an additional 5 K contour); 40 K for SiO; and 5 K for all the other lines; the dust contours are the same as in Figure 1. The positions of radio sources BN and I are marked by filled squares.

Fig. 4.— Comparison of SO, SiO v=0 and $H^{13}CN$ emission at $1''.7\times0''.7$ resolution. The SO emission is shown by the gray scale in both panels; the line is integrated over the velocity interval $10 < V_{LSR} < 14$ km s^{-1}. Contours in the left panel show SiO v=0 emission, integrated over $-20 < V_{LSR} < 25$ km s^{-1}; the contour levels are 27, 68, 136, 272, 408, and 544 K. Contours in the right panel show $H^{13}CN$ emission, integrated over $2.6 < V_{LSR} < 13.8$ km s^{-1}; the contour levels are 23, 46, 69, 93, 116, 139, and 162 K. The filled square marks the position of source I.

Fig. 5.— Position–velocity maps along position angle 23° derived from $H^{13}CN$, HC_3N, SO, and CH_3CN data. The outflow from IRc2 is responsible for the broad velocity emission near the center of each cut. Thick lines show the rotation curve obtained by Vogel et al. (1984). For CH_3CN we used the velocity scale for the K=0 transition, and the rotation curve is only shown for this velocity.

Fig. 6.— Maps of molecular line emission from Orion over the velocity range $9.5 < V_{LSR} < 11.5$ km s^{-1}, characteristic of the northern ridge cloud (CS1). The contour intervals are 3 K for DCN and H_2CO; 5 K for HC_3N, CH_3CN, and CH_3OH; and 15 K for $H^{13}CN$. Crosses mark the positions of the hot core, western clump, and CS1 dust peaks (from Wright et al. 1992).

Fig. 7.— Spectra of $H^{13}CN$, HC_3N, CH_3CN, and CH_3OH toward the northern cloud at $5 \times 7''$ resolution ($11''.1$ E, $25''.4$ N of source I).

Fig. 8.— Evidence that the outflow from KL impinges on the southern edge of CS1. Gray scale shows the 450 micron dust continuum image from Wright et al. (1992); the peak brightness

temperature is 19 K and the resolution is 8″. Solid contours show the HC_3N, CH_3OH, CH_3CN (K=3), and SO molecular line emission, integrated over a the velocity range $6.5 < V_{LSR} < 11.5$ km s^{-1}. The contour intervals and beam sizes are: SO (10 K; 3.″9×3.″2), HC_3N (4 K; 6.″4×5.″2), CH_3CN (K=3) (3.9 K, and then from 7.8 K at 7.8 K intervals; 7.″3×5.″1), CH_3OH (3.9 K, and then from 11.6 K at 7.7 K intervals; 7.″1×4.″9). In the bottom left panel, dashed contours show the 2 micron H_2 v=1–0 S(1) emission at 6″ resolution (Beckwith et al. 1978); in the bottom right panel, white crosses indicate H_2O masers (Genzel et al. 1981). A white square marks the position of source I.

Fig. 9.— Images of the hot core at 1.″7×0.″8 resolution. (a) 86 GHz dust continuum, contour interval 1 K. (b) $HC^{15}N$ (86.055 GHz), contour interval 10 K. (c) NH_2D (85.926 GHz), contour interval 8 K. (d) SiO v=0 (Wright et al. 1995), contour interval 250 K. A triangle marks the location of radio continuum source I.

Fig. 10.— Solid contours are $H^{13}CN$ emission at 1.″7×0.″8 resolution, integrated over the velocity range $9 < V_{LSR} < 11$ km s^{-1} to show the hot core, western clump and north cloud. The contour levels are 26, 52, 79, 105, 131, 157, 210 K. Dashed, shaded contours show 3.8 micron emission (Dougados et al. 1993) at 0.″5 resolution, with contour interval 3.5 mJy/beam; the peak flux is 13.9 Jy/beam. BN and source I are marked by a star and a filled square respectively. The maps were aligned w.r.t. the radio position of BN.

Fig. 11.— Comparison of the low velocity outflow mapped in SO_2 (top panels) and SO (bottom panels) at velocities between 2 and 19 km s^{-1}; each map covers a 5 km s^{-1} wide velocity interval. The contour interval is 1 Jy/beam, 13.5 and 13.2 K for SO_2 and SO respectively. Crosses on the SO_2 maps indicate the positions of H_2O masers (Genzel et al. 1981).

Fig. 12.— SO position–velocity map at position angle 135° through source I at 1.″2 resolution. The offset is positive to the SE, in a direction towards the hot core. Contours at intervals 15, 30, 45, 60, 75, 90 percent of the maximum intensity, 1.5 Jy/beam (182 K).

Fig. 13.— Comparison of the high velocity outflow mapped in HCN, CO, SO_2, SO, and SiO at velocities more than 20 km s^{-1} from V_{LSR}=9 km s^{-1}. Solid contours indicate blueshifted emission ($V_{LSR} < -11$ km s^{-1}); dashed contours, redshifted emission ($V_{LSR} > 29$ km s^{-1}). The contour interval is 4 K. A filled square marks the position of source I. In the upper right panel, solid contours show the SiO v=0 emission at 0.″7×1.″7 resolution, integrated over a 50 km s^{-1} velocity interval; the peak brightness temperature is 480 K. Dashed contours in the upper right panel show 2 micron H_2 v=1-0 S(1) emission at 6″ resolution (Beckwith et al. 1978), while crosses show H_2O masers (Genzel et al. 1981).

Fig. 14.— Overlay of HC_3N (contours) and SO (gray scale) maps in 1 km s^{-1} intervals centered at V_{LSR} 4, 8, 12 and 16 km s^{-1}. The contour interval is 5.5 K; grey scale from 13 to 91 K. The SO appears to lie around the edges of the HC_3N clumps in these narrow velocity intervals.

Fig. 15.— 3mm dust image showing positions for abundance calculations. The contour interval is 50 mJy/beam with a $5'' \times 7''$ beam (0.26 K) Positions (x,y) arcsecs to the east and north of source I are: (11.10, 25.40), (7.60, 13.90), (1.60, 5.90), (0.60, -1.10), (-5.40, 3.90), (-8.40, -7.10), (-8.40, -15.10), (2.60, -10.10), (11.60, -9.10)

Fig. 16.— Graphical depiction of derived column densities listed in Table 4 for each species in three Gaussian components at the 9 nine positions shown in Figure 15.

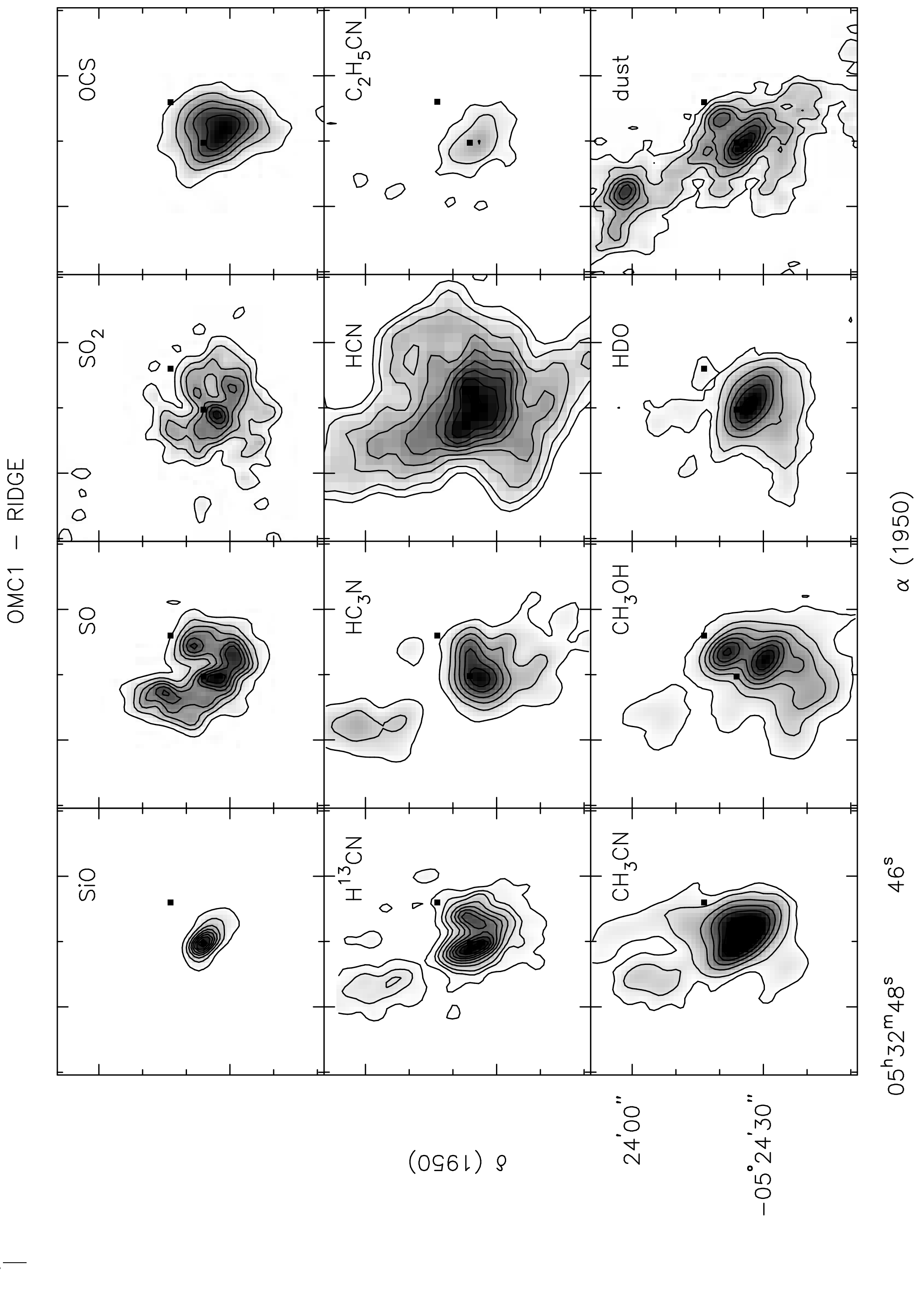
OMC1 – RIDGE
SiO
SO
SO$_2$
OCS
H^{13}CN
HC$_3$N
HCN
C$_2$H$_5$CN
CH$_3$CN
CH$_3$OH
HDO
dust
α (1950)
δ (1950)
05^{h}32^{m}48^s
46^s
24′00″
−05°24′30″

Fig. 1.—

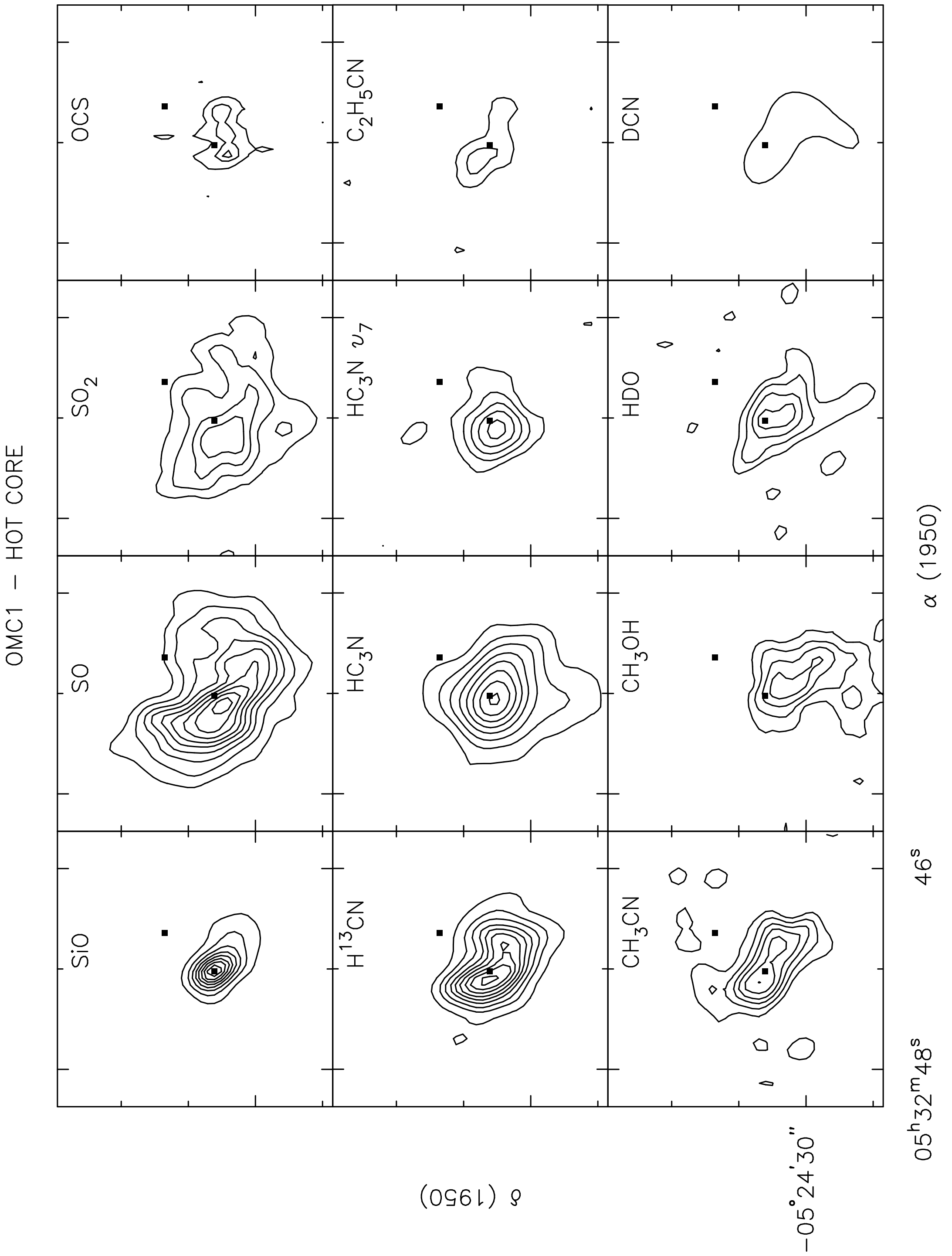
OMC1 – HOT CORE
SiO
SO
SO$_2$
OCS
H^{13}CN
HC$_3$N
HC$_3$N ν_7
C$_2$H$_5$CN
CH$_3$CN
CH$_3$OH
HDO
DCN
α (1950)
δ (1950)
46^s
05^{h}32^{m}48^s
−05°24′30″

Fig. 2.—

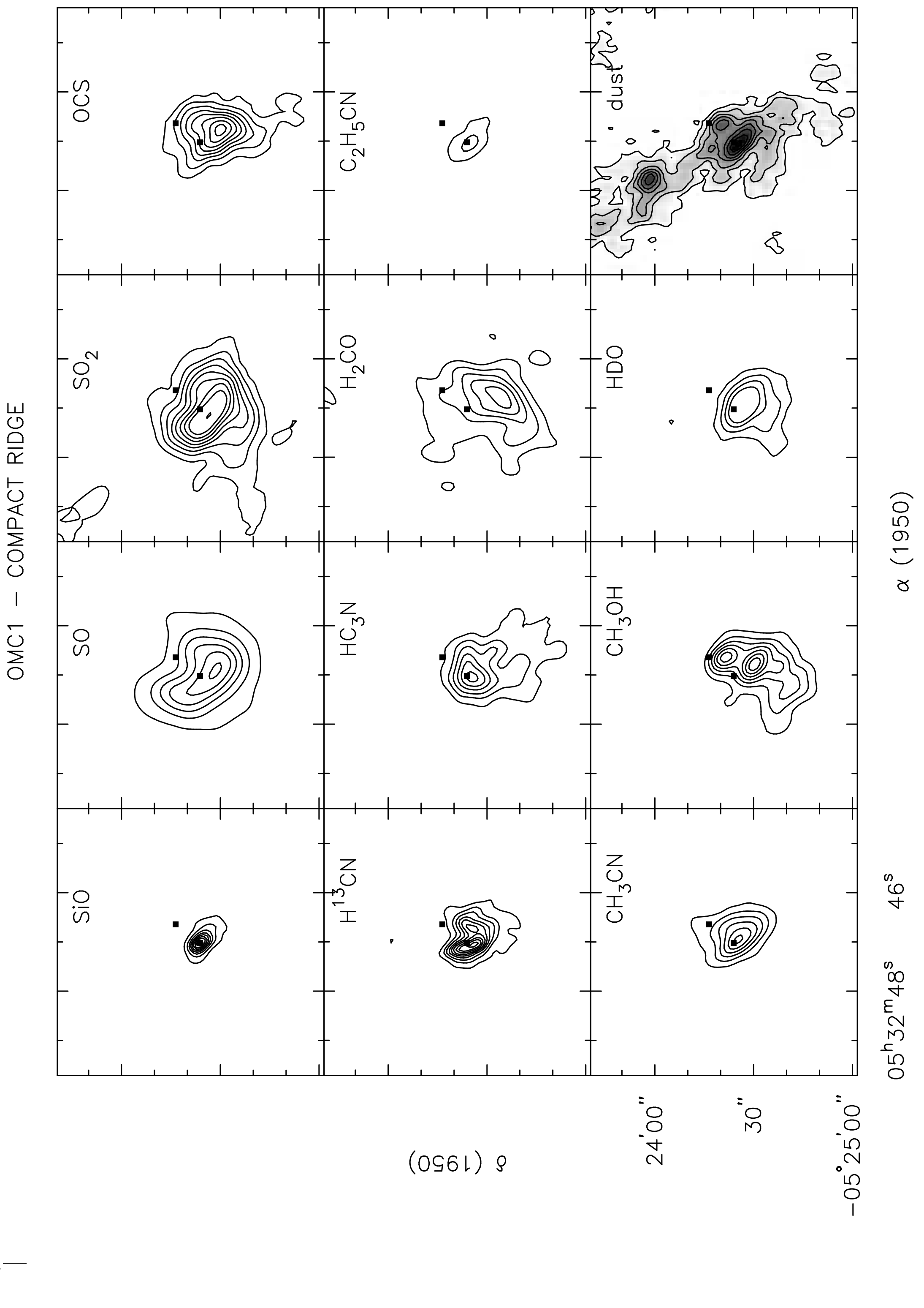
OMC1 – COMPACT RIDGE
SiO
SO
SO2
OCS
H13CN
HC3N
H2CO
C2H5CN
CH3CN
CH3OH
HDO
dust
α (1950)
δ (1950)
05h32m48s
46s
24'00"
30"
−05°25'00"

Fig. 3.—

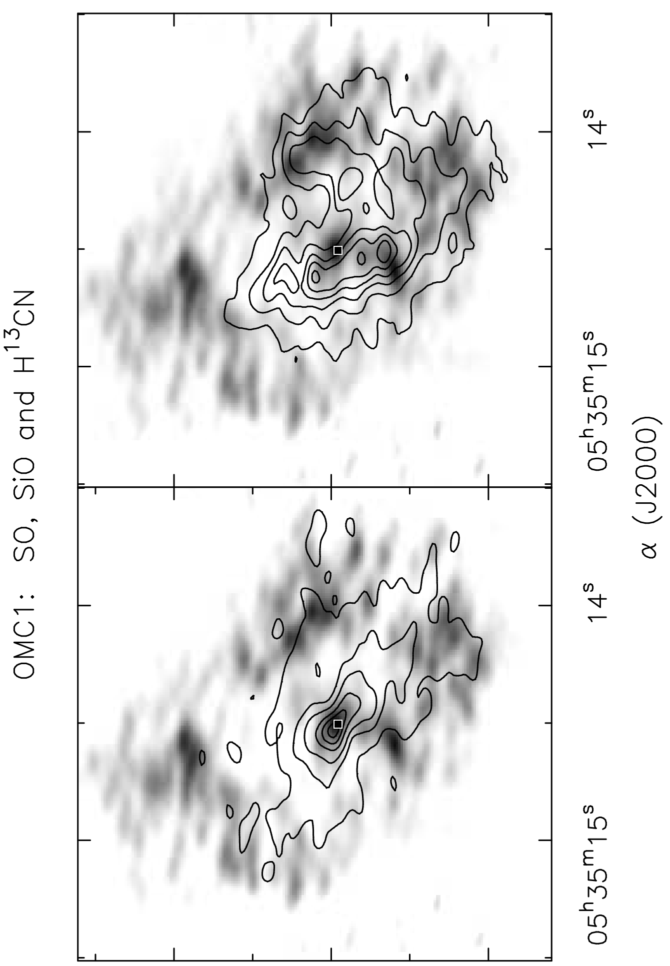
OMC1: SO, SiO and H^{13}CN
20
30
−05 22 40
δ (J2000)
05^{h}35^{m}15^s
14^s
α (J2000)

Fig. 4.—

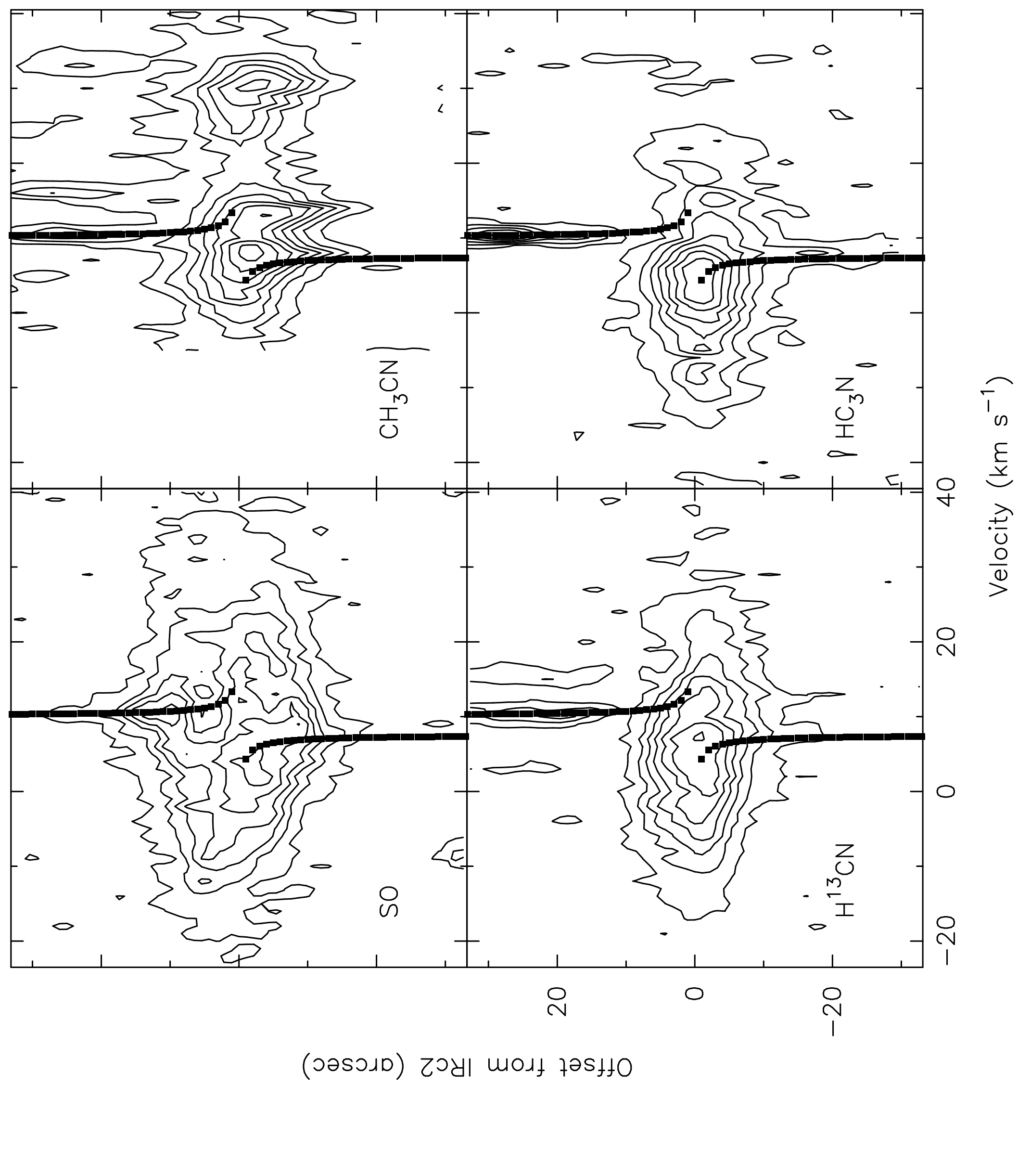
SO
CH$_3$CN
H^{13}CN
HC$_3$N
Velocity (km s^{-1})
Offset from IRc2 (arcsec)
−20
0
20
40
20
0
−20

Fig. 5.—

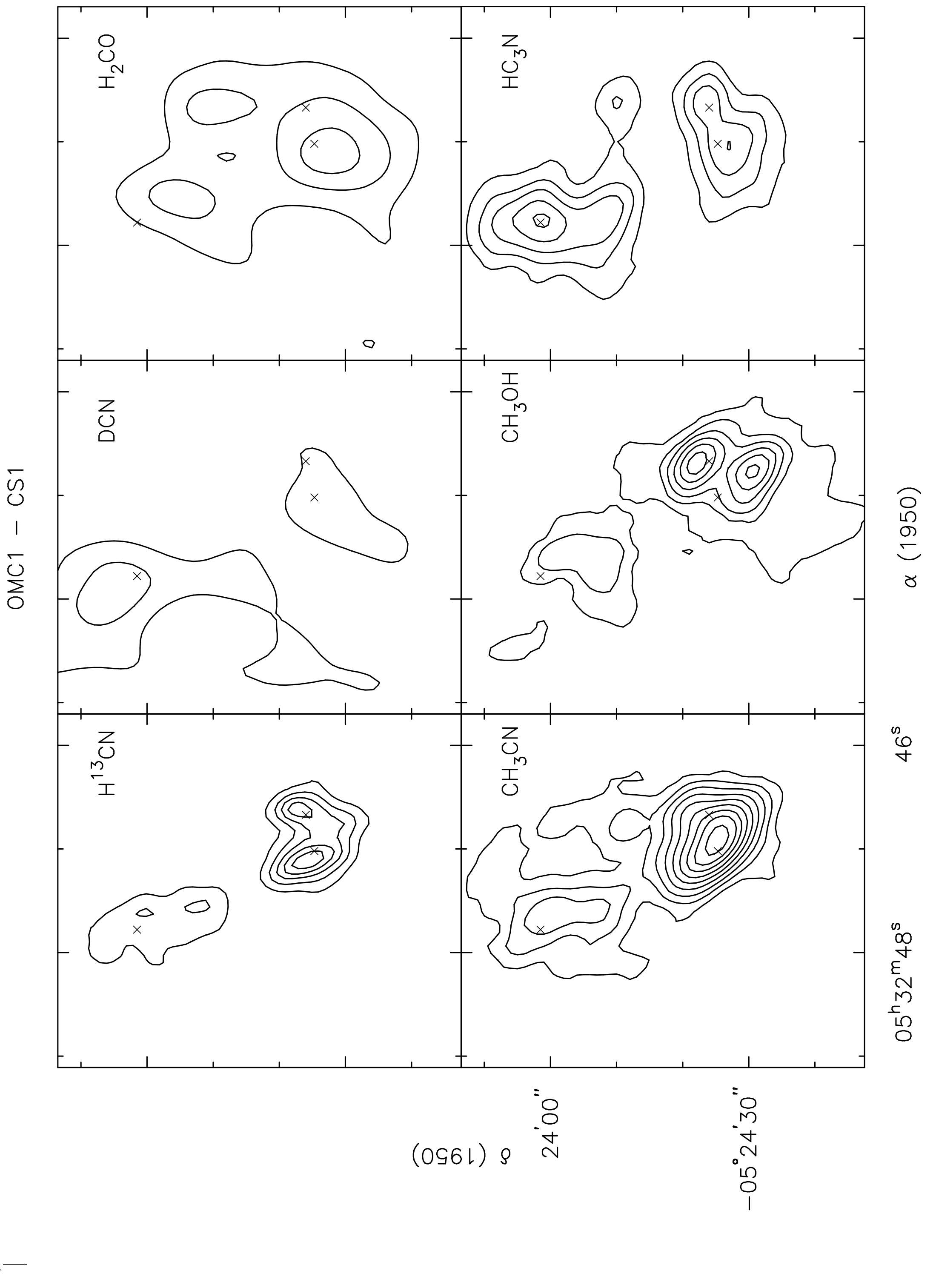
OMC1 – CS1
H2CO
DCN
H13CN
HC3N
CH3OH
CH3CN
α (1950)
δ (1950)
46s
05h32m48s
24'00"
−05°24'30"

Fig. 6.—

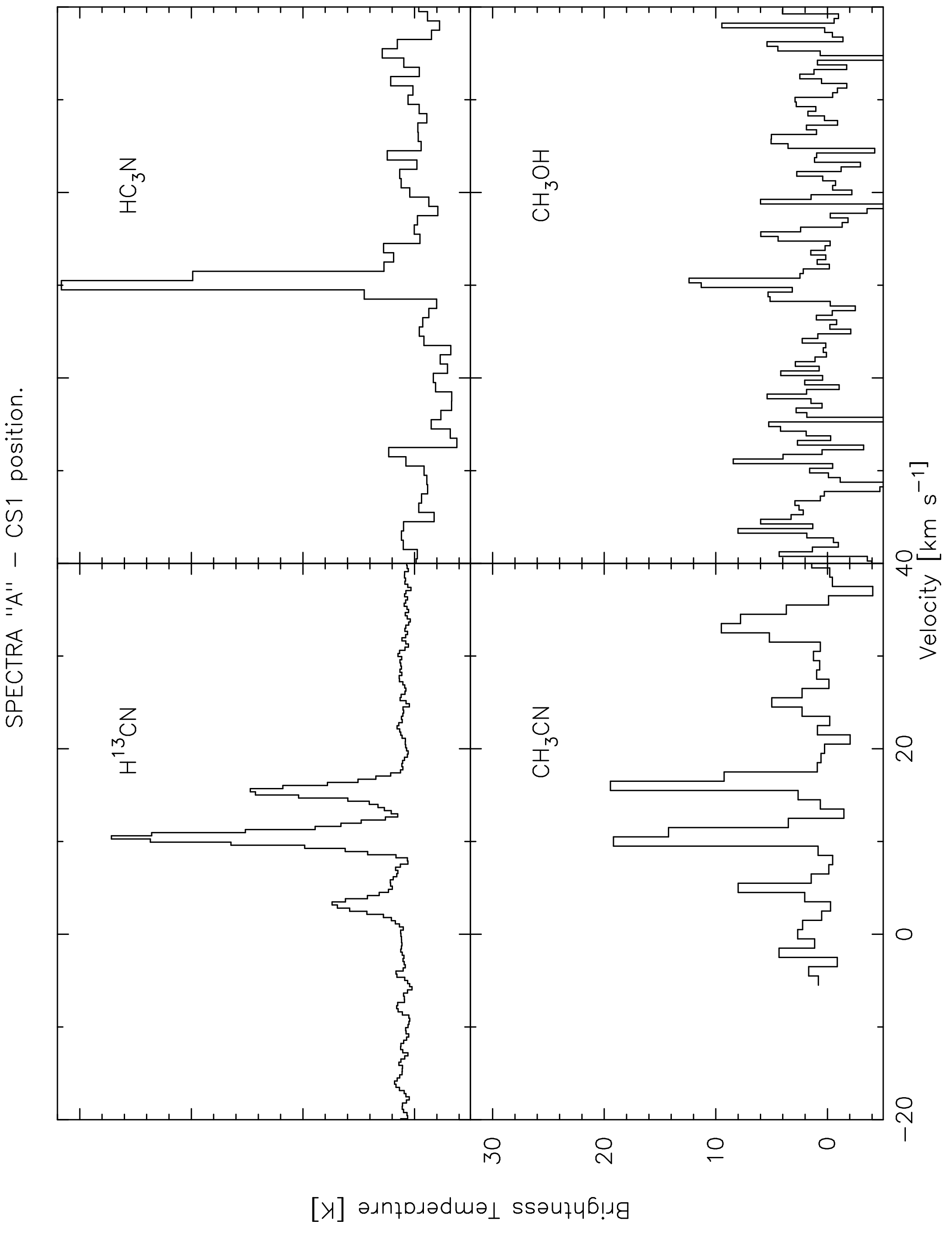
SPECTRA "A" – CS1 position.
H13CN
HC3N
CH3CN
CH3OH
Velocity [km s-1]
Brightness Temperature [K]
−20
0
20
40
0
10
20
30

Fig. 7.—

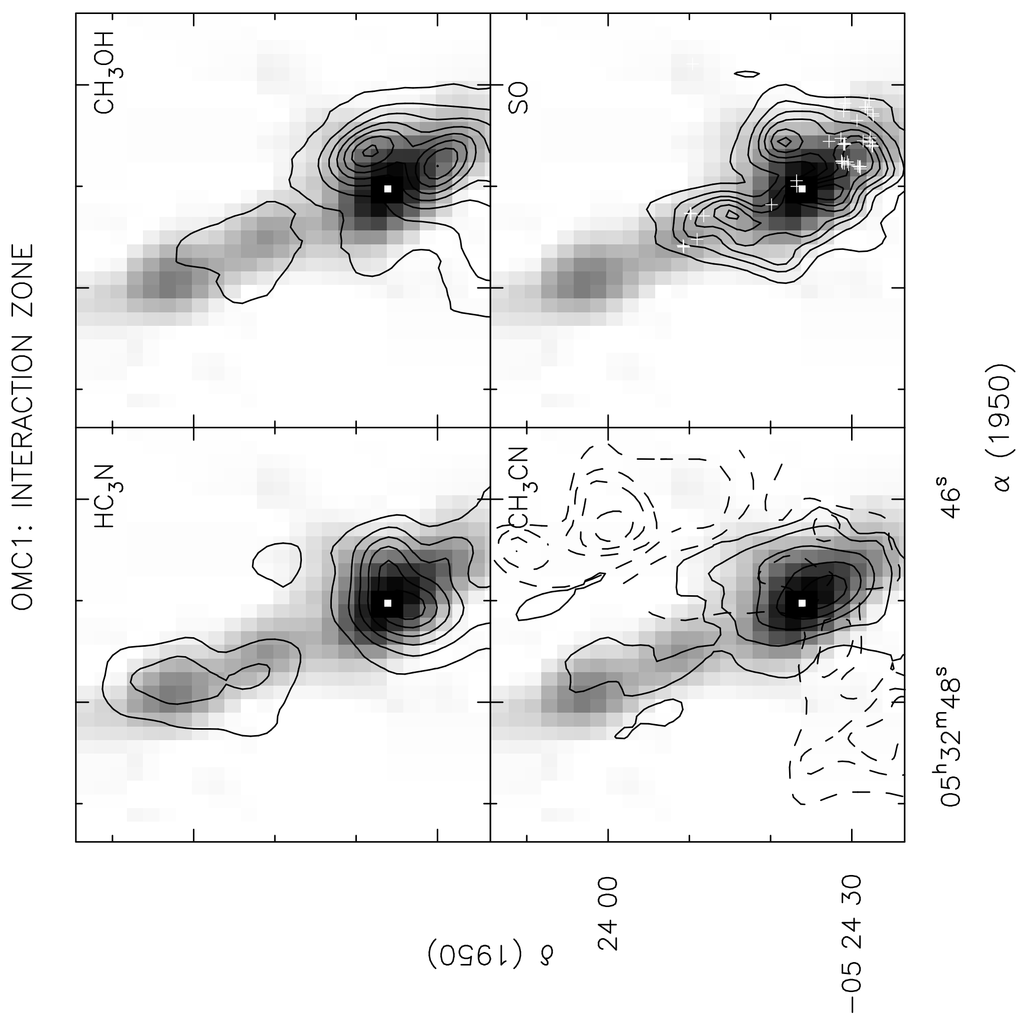

OMC1: INTERACTION ZONE
HC3N
CH3OH
CH3CN
SO
24 00
−05 24 30
δ (1950)
05h32m48s
46s
α (1950)

Fig. 8.—

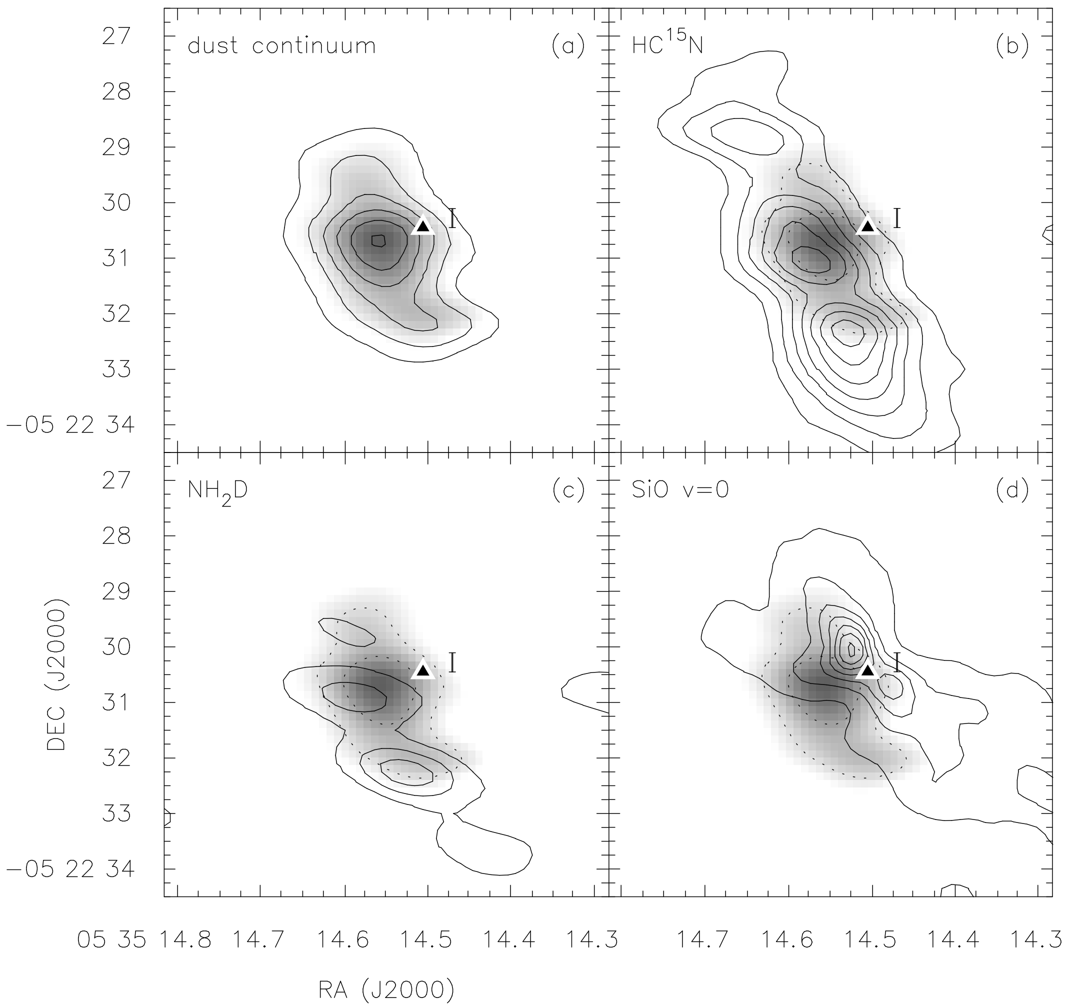
dust continuum
(a)
HC^{15}N
(b)
NH$_2$D
(c)
SiO v=0
(d)
I
DEC (J2000)
27
28
29
30
31
32
33
−05 22 34
05 35 14.8
14.7
14.6
14.5
14.4
14.3
RA (J2000)

Fig. 9.—

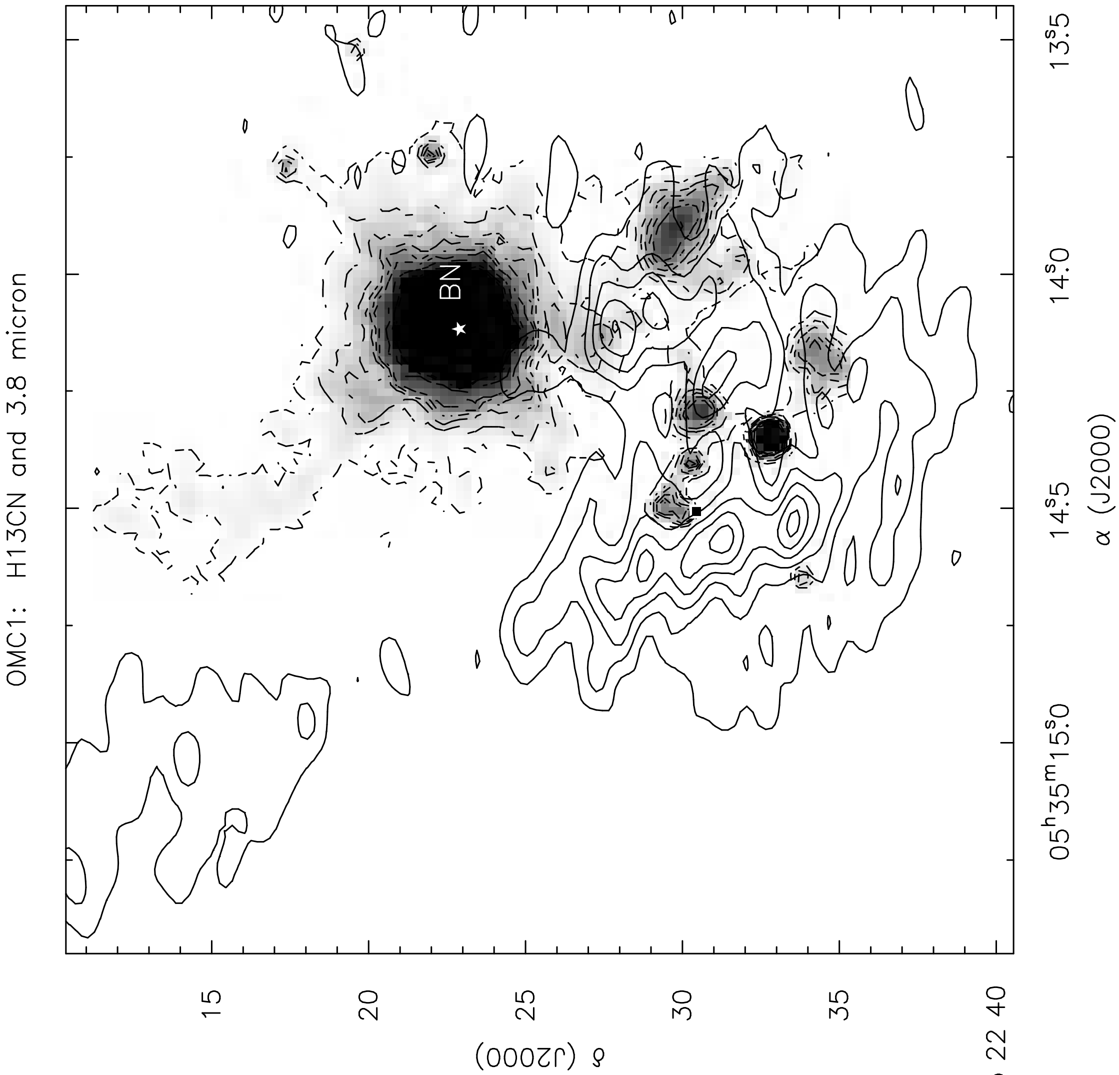

OMC1: H13CN and 3.8 micron
BN
α (J2000)
δ (J2000)
05h35m15s.0
14s.5
14s.0
13s.5
−05 22 40
35
30
25
20
15

Fig. 10.—

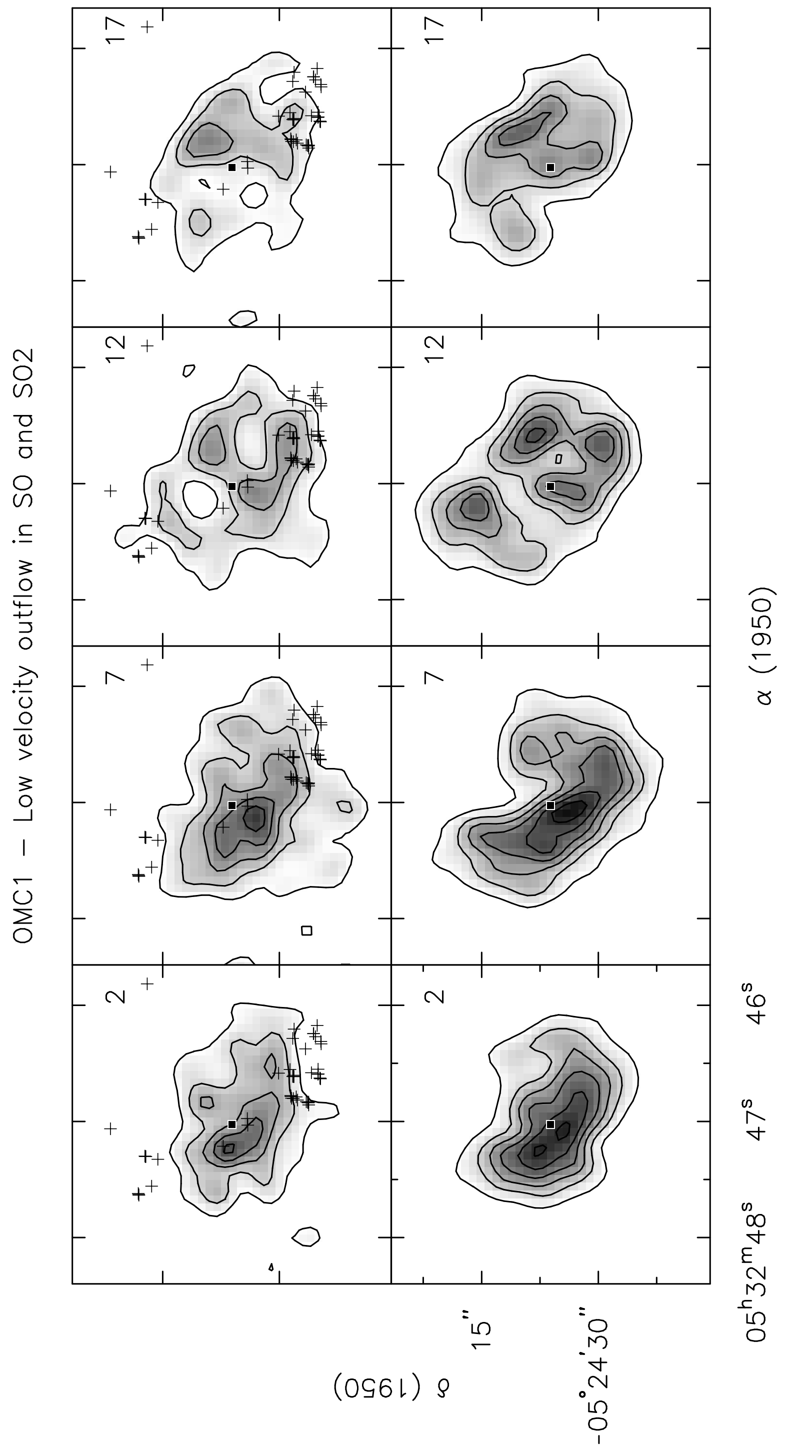
OMC1 – Low velocity outflow in SO and SO2
2
7
12
17
α (1950)
δ (1950)
$05^h32^m48^s$
47^s
46^s
$-05°24'30''$
$15''$

Fig. 11.—

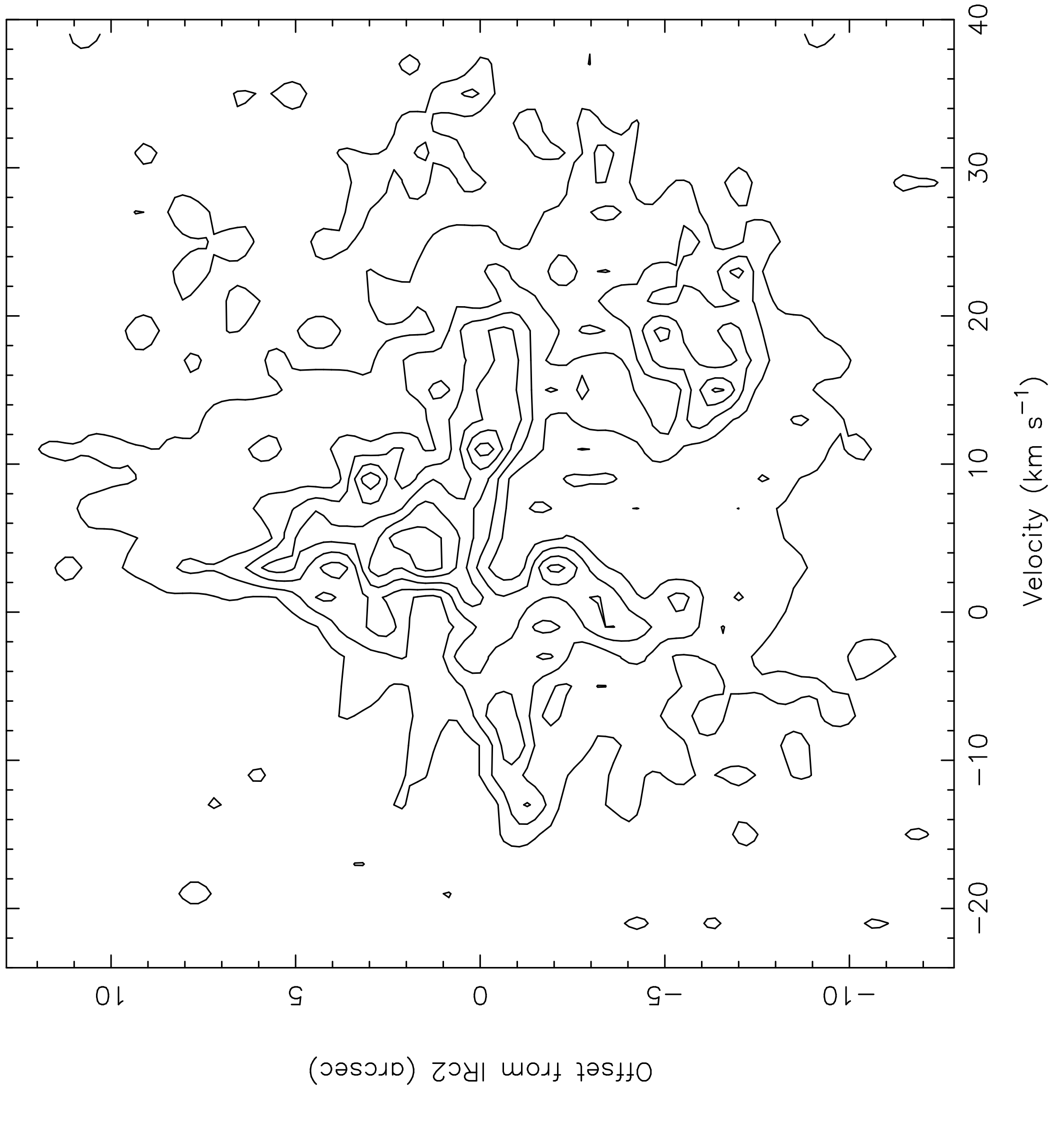
Velocity (km s^{-1})
Offset from IRc2 (arcsec)
40
30
20
10
0
−10
−20
10
5
0
−5
−10

Fig. 12.—

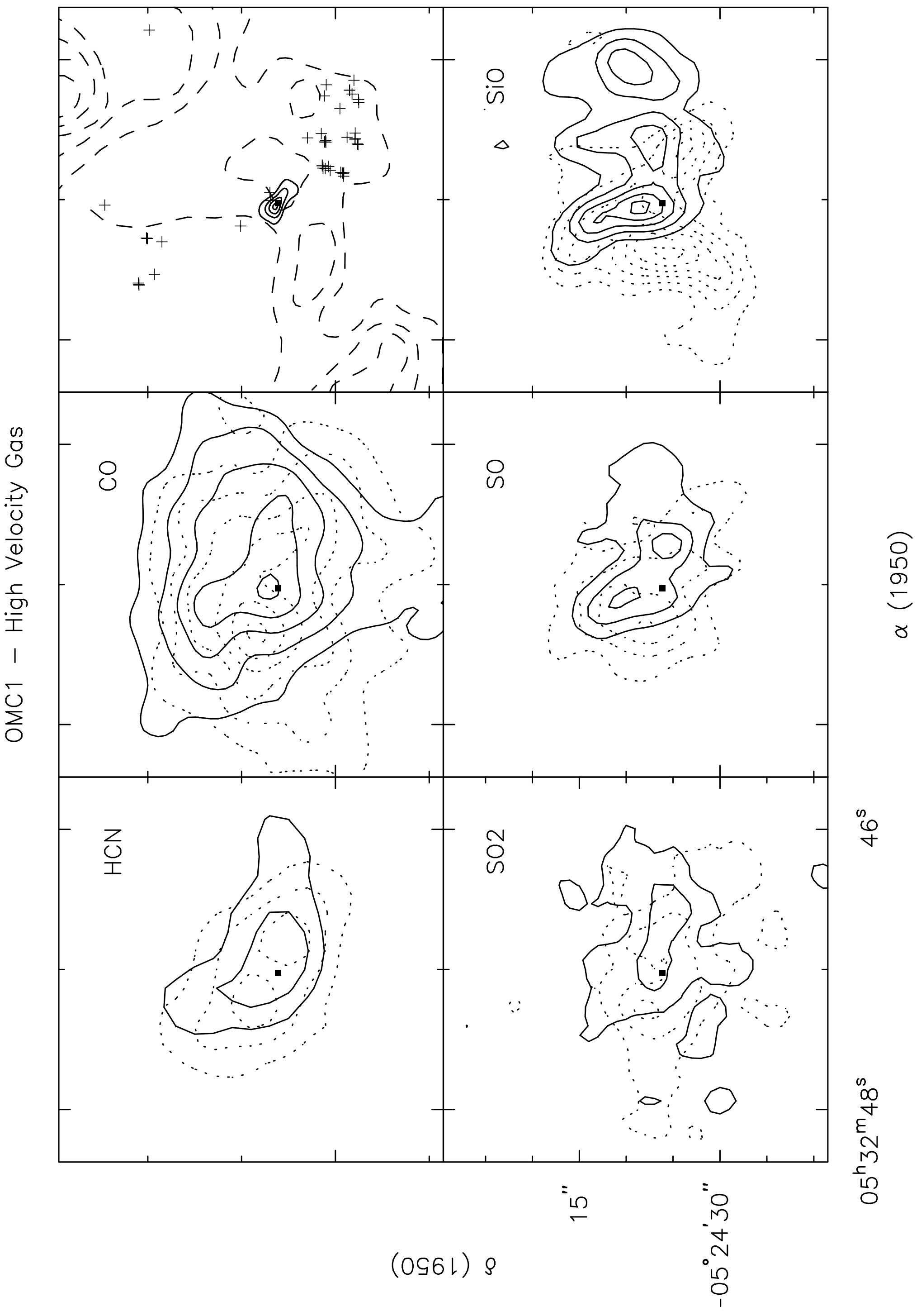
OMC1 – High Velocity Gas
HCN
CO
SO2
SO
SiO
α (1950)
δ (1950)
15″
-05°24′30″
05h32m48s
46s

Fig. 13.—

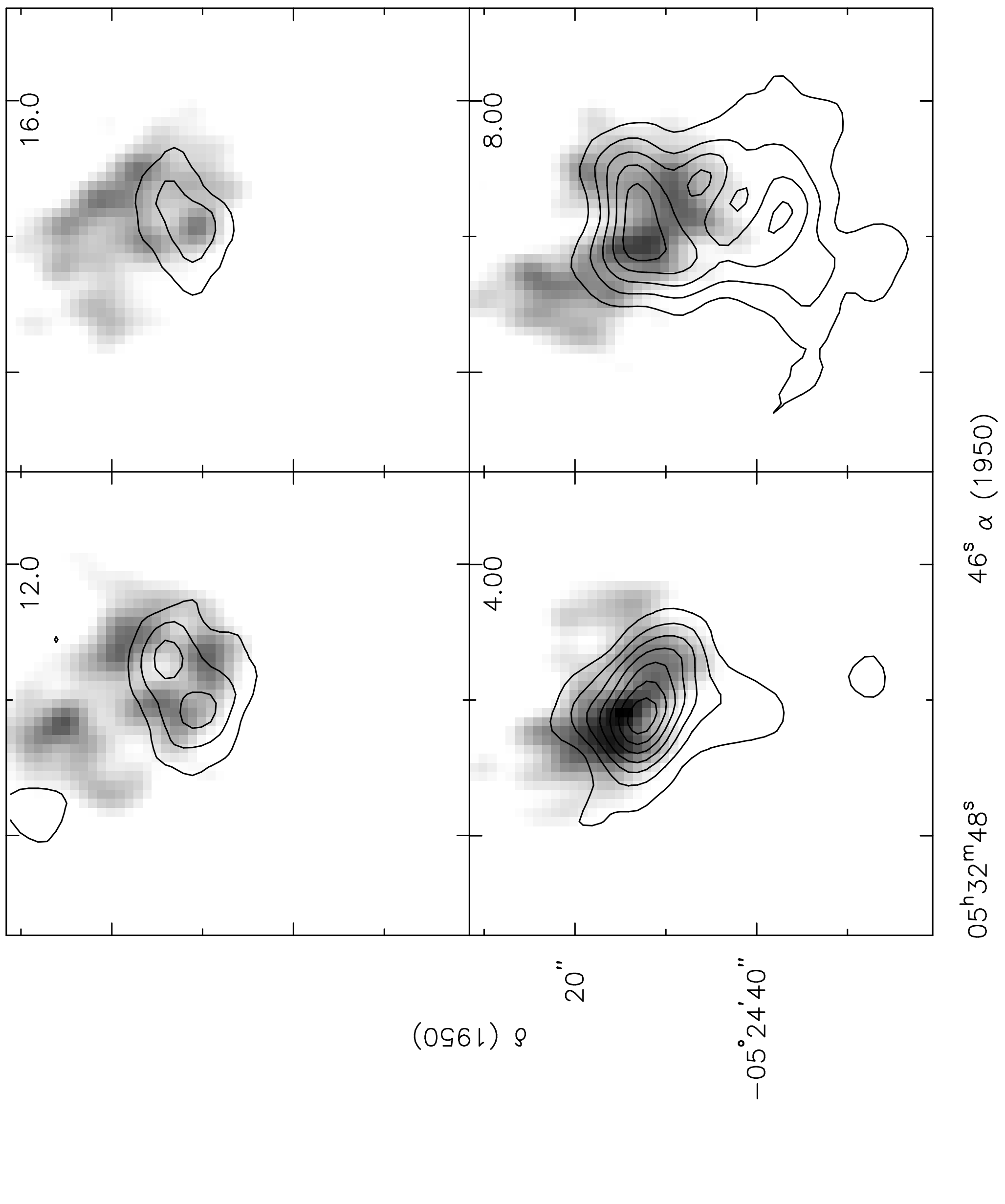
OMC1 – SO and HC3N
16.0
12.0
8.00
4.00
05h32m48s
46s α (1950)
δ (1950)
20"
−05°24'40"

Fig. 14.—

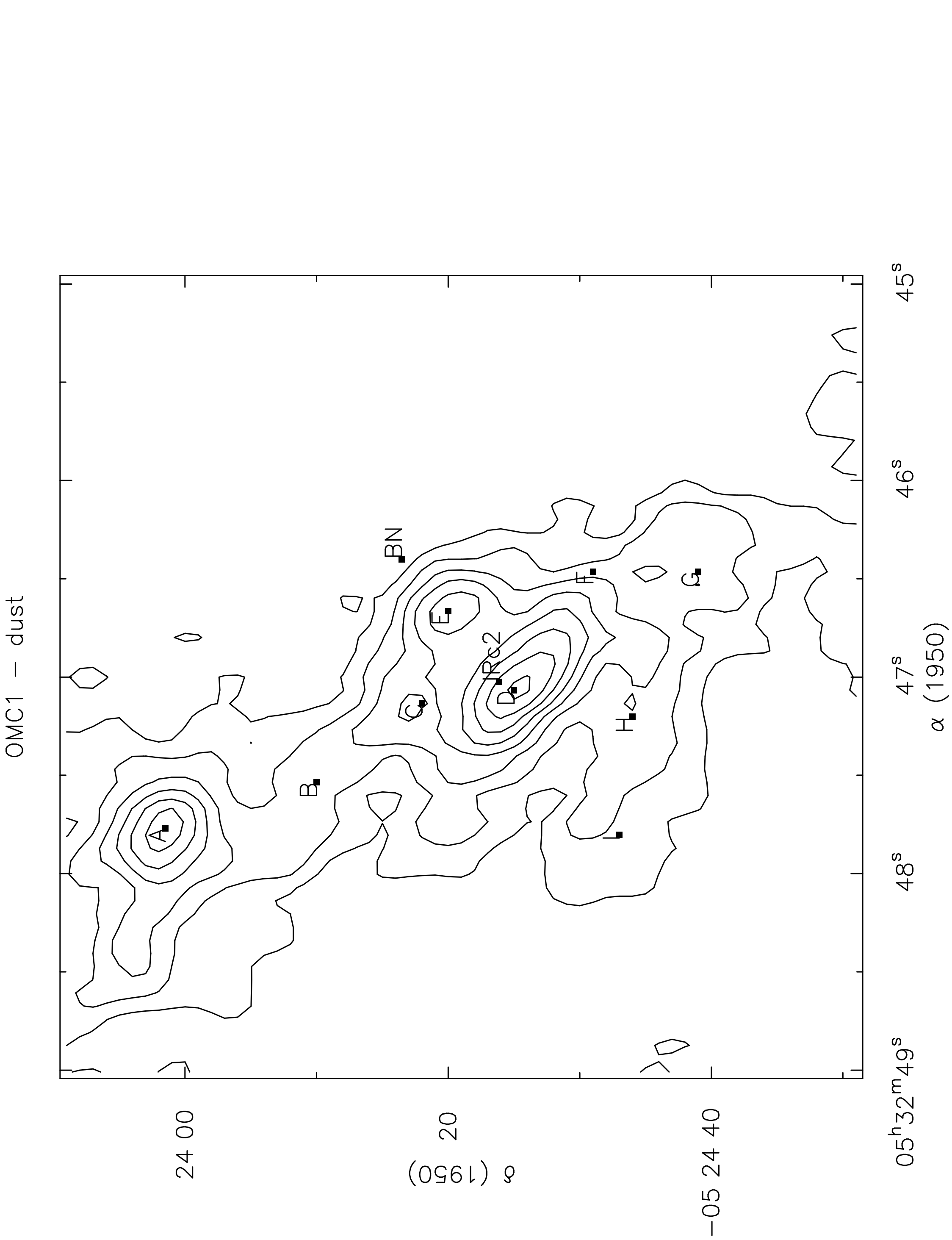
OMC1 – dust
BN
E
IRc2
D
C
F
G
H
I
B
A
45s
46s
47s
48s
05h32m49s
α (1950)
24 00
20
−05 24 40
δ (1950)

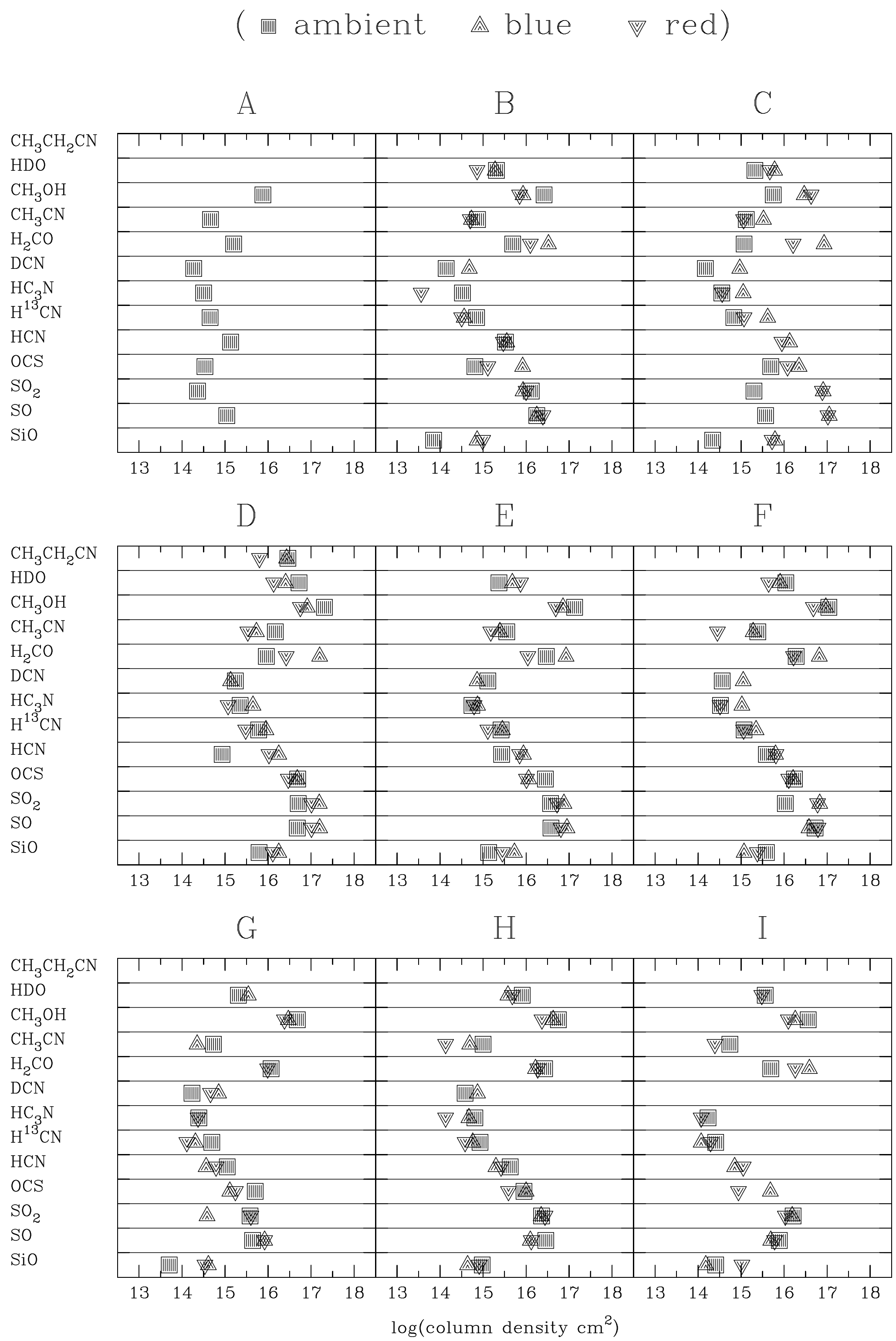
(ambient blue red)
A
B
C
D
E
F
G
H
I
CH3CH2CN
HDO
CH3OH
CH3CN
H2CO
DCN
HC3N
H13CN
HCN
OCS
SO2
SO
SiO
13 14 15 16 17 18
log(column density cm2)